High-order linear and non-linear residual distribution schemes for turbulent compressible flows

Dante de Santis

High-order linear and non-linear residual distribution schemes for turbulent compressible flows

D. De Santis[a]

[a]*INRIA Bordeaux–Sud-Ouest, Équipe-projet Bacchus, 200 avenue de la Vieille Tour, 33405 Talence Cedex, France*

Abstract

A high-order Residual Distribution scheme for the solution of the compressible RANS equations is developed. The one-equation Spalart-Allmaras turbulence model is solved in a fully coupled approach; the mean flow equations as well as the turbulence equation are solved with high-order of accuracy. A continuous approximation of the solution is adopted and standard Lagrangian basis functions are used to construct the discrete space. Since viscous terms involve the gradient of the numerical solution which has a discontinuous normal component across the faces of the elements, a continuous approximation of the gradient of the numerical solution is recovered at each degree of freedom of the grid and then interpolated with the same basis functions used for the solution. The non-linear system of equations resulting from the numerical discretization is solved with the non-linear LU-SGS method. Several numerical experiments are performed to verify the accuracy of the numerical method, these are based on both subsonic and transonic flows in two and three spatial dimensions.

Keywords: High order schemes, residual distribution, gradient reconstruction, RANS equations, implicit method

1. Introduction

The majority of the CFD tools used for aerodynamic simulations in the aeronautical industry is based on theoretically second-order Finite Volume (FV) methods [1], whose order of accuracy in practice ranges between one and two due to irregular and highly stretched meshes used. In order to obtain mesh independent solutions very fine meshes with a very large number of degrees of freedom are required, which lead to enormous computational times. High-order methods have the potential to achieve a faster reduction of the discretization errors, maintaining limited the increment of the computational effort.

Probably, one of the most popular scheme in the high-order community is the Discontinuous Galerkin (DG) method [2], which is very attractive for its compactness and flexibility. On the other hand DG methods suffer from the serious drawback of a very fast growth of the number of degrees of freedom (DOFs) with the cell polynomial degree, making these schemes very expensive. Furthermore, the treatment of discontinuities in the DG framework is still not clear and the non-oscillatory properties of DG schemes are still not well understood. An interesting alternative to DG schemes is represented by Residual Distribution (RD) methods. In the RD framework the solution is continuous and the number of DOFs is much lower than DG methods for the same order of approximation of the solution. Furthermore, in the RD framework is very clear how to construct non-linear schemes, which overcome the Godunov's barrier and can be at the same time high-order accurate in smooth regions and monotone across the discontinuities.

The basic idea of the RD approach is to define for each element an integral quantity (the total residual) which is the integral over the element of the governing equations. Such quantity is then distributed to the DOFs of the elements. The way the distribution process is performed determines the behavior of the numerical scheme. For example, in the past, truly multidimensional schemes have been developed. In these schemes, for each element, only upwind nodes can receive a contribution in the distribution process, while downwind nodes receive no contribution [3]. Due to this multidimensional character, these schemes are much more accurate that standard second-order FV methods.

Email address: dante.de_santis@inria.fr (D. De Santis)

The drawback of the multidimensional upwind schemes is that the extension to orders of accuracy more than two and to non simplex elements is not straightforward, due to the fact that the construction of the numerical schemes relies on geometrical considerations. More flexible approaches make use of centered RD schemes in which, for each element, all the DOFs receive a contribution during the distribution process, regardless if they are in the upwind or downwind region. For example, finite element approaches like SUPG [4] or Lax-Wendroff [5] can be interpreted as centered RD schemes. Recently, Abgrall [6] proposed a non-linear RD method in which a simple low-order centered scheme is used as base for the construction of a higher-order scheme that is still monotone near shocks. An additional advantage of this approach is that the numerical method can be easily extended to any order of approximation and to any type of element.

Although the RD discretization of advective problems is very clear, the extension of RD methods to advection-diffusion problems is not straightforward. The simple blending of a RD scheme for advection terms with a Galerkin discretization of the diffusive terms usually produces a sub-optimal scheme in regions where advection and diffusion have the same importance. A different strategy consists in using a single RD scheme for the whole advection-diffusion equation. However, a new difficulty arises due to the fact that, for polynomial piecewise approximation of the solution, the normal component of the gradient of the numerical solution is discontinuous on the face of two adjacent elements. Instead of using a numerical flux for the viscous terms, leading to the introduction of additional parameters that might be difficult to understand, one could think of reconstructing an unique set of values of the gradient of the numerical solution at the DOFs. This set of values is used to interpolate the gradient with the same continuous functions used to interpolate the solution, making straightforward the calculation of the total residual of the whole advection-diffusion equations.

In [7] this approach was studied in detail considering the scalar advection-diffusion problem. In particular different gradient reconstruction strategies were considered and the effect of the gradient reconstruction on the accuracy of the numerical solution was studied. It was found that, in order to preserve the overall accuracy of numerical scheme, the gradient of the numerical solution must be reconstructed with a procedure such that the gradient has the same order of accuracy of the solution. Several gradient reconstruction techniques were considered and it was found that the so-called Super-convergent Patch Recovery method of Zienkiewicz and Zhu [8, 9] (SPR-ZZ) was able to reconstruct the gradient with the optimal accuracy without enlarging the stencil of the numerical scheme.

In [10] the scheme has been extended to the Navier-Stokes equations. Numerical experiments confirmed that the optimal accuracy of the numerical scheme is lost if the gradient of the numerical solution is not properly reconstructed. The SPR-ZZ method has been used in the contest of the Navier-Stokes equations to construct linear and non-linear RD schemes for the discretization of steady laminar flows at the second and third order of accuracy.

In this work the RD numerical solver is extended to RANS equations, showing how high-order RD schemes might be very effective to get highly accurate solutions with a reduced number of DOfs than a lower-order discretization. In particular, non-linear RD schemes might be very attractive for simulations of transonic turbulent flows, because no artificial viscosity is required to get monotone solutions near discontinuities.

The structure of the paper is as follows. In Section 2, the multidimensional RANS equations with the Spalart-Allmaras turbulence model fully coupled with the mean flow equations are described. In Section 3, the proposed RD method for advection-diffusion problems is described. The detail of the construction of linear and non-linear schemes are given. In Section 4, the strategy used to reconstruct the gradient is described in detail. In Section 5, is described the construction a non-linear LU-SGS method for a robust and effective implicit scheme. In Section 6, numerical experiments are reported; both subsonic and transonic flows in two and three spatial dimensions are considered. Finally, a few conclusions are drawn in Section 7.

2. Governing equations

The compressible Reynolds Averaged Navier-Stokes (RANS) equations coupled with the one equation Spalart-Allmaras turbulence model [11] can be written in the following conservative form

$$\begin{aligned}
&\frac{\partial \rho}{\partial t} + \boldsymbol{\nabla}\cdot \boldsymbol{m} = 0 \\
&\frac{\partial \boldsymbol{m}}{\partial t} + \boldsymbol{\nabla}\cdot\left(\frac{\boldsymbol{m}\otimes\boldsymbol{m}}{\rho} + P\mathbb{I}\right) = \boldsymbol{\nabla}\cdot\mathbb{S} \\
&\frac{\partial E^t}{\partial t} + \boldsymbol{\nabla}\cdot\left((E^t + P)\frac{\boldsymbol{m}}{\rho}\right) = \boldsymbol{\nabla}\cdot\left(\mathbb{S}\cdot\frac{\boldsymbol{m}}{\rho} - \boldsymbol{q}\right) \\
&\frac{\partial \mu_t^\star}{\partial t} + \boldsymbol{\nabla}\cdot\left(\mu_t^\star\frac{\boldsymbol{m}}{\rho}\right) = \boldsymbol{\nabla}\cdot\left(\frac{\eta}{\sigma_{SA}}\boldsymbol{\nabla}\left(\frac{\mu_t^\star}{\rho}\right)\right) + S_{SA},
\end{aligned} \tag{1}$$

where the unknowns are the density ρ, the momentum vector $\boldsymbol{m}$, the total energy per unit volume E^t and the turbulent working variable $\mu_t^\star$, with

$$\boldsymbol{m} = \rho\boldsymbol{v} \quad \text{and} \quad E^t = \rho e + \frac{\|\boldsymbol{m}\|^2}{2\rho},$$

where $\boldsymbol{v}$ is the velocity vector and e is the specific (*i.e.*, for unit of mass) internal energy. Furthermore, in the system (1) P is the static pressure, $\mathbb{I} \in \mathbb{R}^{N_{\text{dim}}}$ is the identity matrix, with N_{dim} number of spatial dimensions, $\mathbb{S}$ is the viscous stress tensor and $\boldsymbol{q}$ is the heat flux vector. The viscous stress tensor can be written as

$$\mathbb{S} = -\frac{2}{3}(\mu + \mu_t)(\boldsymbol{\nabla}\cdot\boldsymbol{v})\mathbb{I} + (\mu + \mu_t)(\boldsymbol{\nabla}^{\mathrm{T}}\boldsymbol{v} + \boldsymbol{\nabla}\boldsymbol{v}),$$

where μ is the fluid dynamic viscosity and μ_t is the turbulent eddy viscosity, which is given by

$$\mu_t = \begin{cases} \mu_t^\star f_{v1}, & \mu_t^\star > 0, \\ 0, & \mu_t^\star \leq 0, \end{cases} \tag{2}$$

where

$$f_{v1} = \frac{\chi^3}{\chi^3 + c_{v1}^3}, \quad \text{with} \quad \chi = \frac{\mu_t^\star}{\mu_t}, \quad c_{v1} = 7.1.$$

The heat flux, using the Fourier law, can be written as: $\boldsymbol{q} = -(\kappa + \kappa_t)\boldsymbol{\nabla}T$, where T is the temperature and the thermal conductivity is evaluated using the constant Prandtl number hypothesis

$$\kappa = c_p\frac{\mu}{Pr}, \quad \text{and} \quad \kappa_t = c_p\frac{\mu_t}{Pr_t},$$

with c_p the specific heat at constant pressure, Pr the laminar Prandtl number and Pr_t the turbulent Prandtl number. Here, $Pr = 0.72$ and $Pr_t = 0.9$.

In the Spalart-Allmaras equation $\eta = \mu + \mu_t$ and $\sigma_{SA} = 2/3$, while the source term is defined as follows

$$S_{SA} = c_{b1}\hat{\omega}\mu_t^\star - \rho c_{w1} f_w\left(\frac{\mu_t^\star}{\rho\, d_{\min}}\right)^2 + \frac{1}{\sigma_{SA}}\rho c_{b2}\left\|\boldsymbol{\nabla}\left(\frac{\mu_t^\star}{\rho}\right)\right\|^2, \tag{3}$$

the three terms in the source term represent respectively the production, the destruction and the diffusion. In the production term, the modified vorticity function is defined as

$$\hat{\omega} = \|\boldsymbol{\omega}\| + \bar{\omega}$$

where $\|\boldsymbol{\omega}\|$ is the magnitude of the vorticity vector, and

$$\bar{\omega} = \frac{\mu_t^\star f_{v2}}{\rho k^2 d_{\min}^2}, \quad \text{with} \quad f_{v2} = 1 - \frac{\chi}{1 + \chi f_{v1}}.$$

The remaining closure functions are

$$f_w = g\left(\frac{1+c_{w3}^6}{g^6+c_{w3}^6}\right)^{\frac{1}{6}}, \quad g = r + c_{w2}(r^6 - r), \quad r = \frac{\mu_t^\star}{\rho\hat{\omega}k^2 d_{\min}^2},$$

with $d_{\min}$ the minimum distance from the wall, $c_{b1} = 0.1355$, $c_{b2} = 0.622$, $k = 0.41$, $c_{w1} = \frac{c_{b1}}{k^2} + \frac{(1+c_{b2})}{\sigma_{SA}}$, $c_{w2} = 0.3$ and $c_{w3} = 2$.

The system (1) is closed by providing a thermodynamic model for the fluid. In this work only the polytropic ideal gas model is considered, for which the pressure and the temperature can be written as

$$P(e,\rho) = (\gamma - 1)\rho e, \quad \text{and} \quad T(e) = \frac{(\gamma-1)}{\mathcal{R}}e,$$

with $\gamma = c_p/c_v$ the specific heats ratio and $\mathcal{R}$ the gas constant.

If the vector of the conservative variables $\mathsf{u} \in \mathbb{R}^{N_{\text{eq}}}$ is introduced, with N_{eq} the number of equations, the system of equations (1) can be written in a more compact form as follows

$$\frac{\partial \mathsf{u}}{\partial t} + \boldsymbol{\nabla}\cdot\mathbf{f}^a(\mathsf{u}) - \boldsymbol{\nabla}\cdot\mathbf{f}^v(\mathsf{u},\boldsymbol{\nabla}\mathsf{u}) = \mathsf{S}(\mathsf{u},\boldsymbol{\nabla}\mathsf{u}), \tag{4}$$

with

$$\mathsf{u} = \begin{pmatrix} \rho \\ \boldsymbol{m} \\ E^t \\ \mu_t^\star \end{pmatrix}, \quad \mathbf{f}^a = \begin{pmatrix} \boldsymbol{m} \\ \dfrac{\boldsymbol{m}\otimes\boldsymbol{m}}{\rho} + P\mathbb{I} \\ (E^t + P)\dfrac{\boldsymbol{m}}{\rho} \\ \mu_t^\star \dfrac{\boldsymbol{m}}{\rho} \end{pmatrix}, \quad \mathbf{f}^v = \begin{pmatrix} 0 \\ \mathbb{S} \\ \mathbb{S}\cdot\dfrac{\boldsymbol{m}}{\rho} - \boldsymbol{q} \\ \dfrac{\eta}{\sigma_{SA}}\boldsymbol{\nabla}\left(\dfrac{\mu_t^\star}{\rho}\right) \end{pmatrix} \quad \text{and} \quad \mathsf{S} = \begin{pmatrix} 0 \\ 0 \\ 0 \\ S_{SA} \end{pmatrix}.$$

where $\mathbf{f}^a$ and $\mathbf{f}^v$ are the advective and the viscous flux functions, respectively, and S is the source term. For later convenience, it is pointed out here that, since the viscous flux function is homogeneous of degree one with respect to the gradient of the conservative variables, it can be also written as follows

$$\mathbf{f}^v(\mathsf{u},\boldsymbol{\nabla}\mathsf{u}) = \mathbb{K}(\mathsf{u})\boldsymbol{\nabla}\mathsf{u},$$

where the viscous flux Jacobian $\mathbb{K}(\mathsf{u}) \in \mathbb{R}^{N_{\text{eq}}\times N_{\text{dim}}\times N_{\text{eq}}\times N_{\text{dim}}}$ is defined as

$$\mathbb{K}(\mathsf{u}) = \frac{\partial \mathbf{f}^v(\mathsf{u},\boldsymbol{\nabla}\mathsf{u})}{\partial\boldsymbol{\nabla}\mathsf{u}}, \qquad \text{with} \qquad \mathsf{K}_{ij}(\mathsf{u}) = \frac{\partial \mathsf{f}_i^v(\mathsf{u},\boldsymbol{\nabla}\mathsf{u})}{\partial\left(\dfrac{\partial\mathsf{u}}{\partial x_j}\right)}.$$

The steady state case, is obtained by removing the time derivative in Eq. (4). The equations are made dimensionless by taking as reference quantities the density, the speed of sound and the temperature at the free-stream and a characterizing length of the problem.

2.1. Modification of the Spalart-Allmaras model

Although the use of the Spalart-Allmaras turbulence model is quite common in numerical simulations of aerodynamic flows, getting a robust solver is still a challenging task. A very important issue of the Spalart-Allmaras model is the behavior of the turbulent governing equation in zones with a high gradient of the working variable. High values of the gradient are generally found near solid walls, where the turbulent variable rises rapidly from zero to a high value, and in the outer zone of the boundary layer where the turbulent variable rapidly decrease to the free-stream value.

While the space discretization is generally such fine in the near-wall zones that the turbulent variable is computed monotonously, the mesh resolution in the outer part of the boundary layer may be insufficient to resolve the turbulent

field. In this case, the turbulent field shows numerical oscillations with negative values of the turbulent variable, which can make the algorithm unstable.

Negative values of the turbulent working variable are disregarded in the definition of the eddy viscosity (see Eq. (2)), but they can compromise the stability of the numerical solver. Several modifications have been proposed in literature to remedy to the problem caused by negative values of $\mu_t^\star$. Some of them are based on simple clippings in the internal functions of the Spalart-Allmaras equations. These approaches, however, might have a negative effect on the implicit iterative solver. In addition, while these approaches might be effective for FV methods, they are usually not robust enough for high-order schemes.

When $\mu_t^\star$ is negative, the turbulence model equation should be modified in order to remove the destabilizing effects. Some used modifications are based on the idea suggested by Allmaras in [12]. In this approach, one writes the equation for the energy of the negative values of the turbulent working variable and the turbulence model is modified in such a way that the rate of change of the unphysical turbulent energy is negative, see [13] for more details. This approach makes the Spalart–Allmaras equation stable in the zone with negative $\mu_t^\star$ and makes the equation continuous and differentiable at $\mu_t^\star = 0$. However, the modifications remove the negative contribution from the source term by making the production very strong in the negative $\mu_t^\star$ region. Although the modification is mathematically stable, it has been observed in numerical simulations that the strong effect induced by the modifications of the production term can induce strong variations of the residual during the iterative convergence, with a possible solver failure. In order to have a more robust solver, the elimination of negative values of $\mu_t^\star$ must be addressed directly.

In the actual implementation of the Spalart–Allmaras equation, two modifications have been adopted which have shown to be very effective. The first modification consists in replacing the variable χ with the following function [14]

$$\psi_{\mu_t^\star} = \begin{cases} 0.05 \log\left(1 + e^{20\chi}\right), & \chi \leq 10, \\ \chi, & \chi > 10, \end{cases}$$

which has the role to deactivate the production and the destruction terms of the turbulence model equation when $\mu_t^\star$ becomes negative. The function $\psi_{\mu_t^\star}$ is continuous and differentiable for all values of χ as can be observed in Fig. 1. The form of the turbulence model would be identical to the original one with the exception that the variable χ is replaced by $\psi_{\mu_t^\star}$. The second modification consists in getting rid of the diffusion contribution in the source term when $\mu_t^\star \leq 0$.

In conclusion, in the improved version of the Spalart-Allmaras turbulence model equation, the eddy viscosity is given by

$$\mu_t = \mu \psi_{\mu_t^\star} f_{v1}, \tag{5}$$

and the turbulent model equations is written as

$$\frac{\partial \mu_t^\star}{\partial t} + \boldsymbol{\nabla} \cdot \left(\mu_t^\star \frac{\boldsymbol{m}}{\rho} - \frac{\eta}{\sigma_{SA}} \boldsymbol{\nabla}\left(\frac{\mu_t^\star}{\rho}\right) \right) = S_{SA},$$

with $\eta = \mu(1 + \psi_{\mu_t^\star})$ and the source term given by

$$S_{SA} = \begin{cases} c_{b1} \hat{\omega} \mu \psi_{\mu_t^\star} - \rho c_{w1} f_w \left(\dfrac{\mu \psi_{\mu_t^\star}}{\rho\, d_{\min}} \right)^2 + \dfrac{1}{\sigma_{SA}} \rho c_{b2} \left\| \boldsymbol{\nabla}\left(\dfrac{\mu_t^\star}{\rho}\right) \right\|^2, & \chi > 0, \\ c_{b1} \hat{\omega} \mu \psi_{\mu_t^\star} - \rho c_{w1} f_w \left(\dfrac{\mu \psi_{\mu_t^\star}}{\rho\, d_{\min}} \right)^2 & \chi \leq 0, \end{cases} \tag{6}$$

the following modified form of $\hat{\omega}$ is used [15]

$$\hat{\omega} = \begin{cases} \|\boldsymbol{\omega}\| + \bar{\omega}, & \bar{\omega} > -c_{v2} \|\boldsymbol{\omega}\|, \\ \|\boldsymbol{\omega}\| + \dfrac{\|\boldsymbol{\omega}\|(c_{v2}^2 \|\boldsymbol{\omega}\| + c_{v3} \bar{\omega})}{(c_{v3} - 2c_{v2})\|\boldsymbol{\omega}\| - \bar{\omega}}, & \bar{\omega} \leq -c_{v2} \|\boldsymbol{\omega}\|, \end{cases}$$

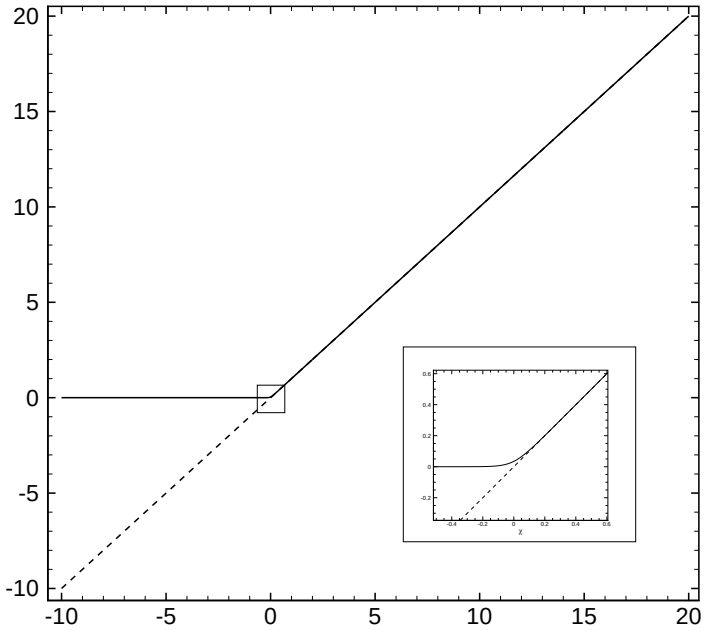

Figure 1: Comparison between $\psi_{\mu_t^\star}$ (solid line) and χ (dashed line) as function of $\mu_t^\star/\mu$.

that is identical to the original expression for $\hat{\omega} > 0.3\|\boldsymbol{\omega}\|$, but remains positive for all nonzero $\|\boldsymbol{\omega}\|$ and is C^1 continuous. The other functions involved in the turbulence model are re-defined as follows

$$\bar{\omega} = \frac{\mu \psi_{\mu_t^\star} f_{v2}}{\rho\, k^2\, d_{\min}^2}, \qquad f_{v1} = \frac{\psi_{\mu_t^\star}^3}{\psi_{\mu_t^\star}^3 + c_{v1}^3}, \qquad f_{v2} = 1 - \frac{\psi_{\mu_t^\star}}{1 + \psi_{\mu_t^\star} f_{v1}},$$

$$f_w = g\left(\frac{1 + c_{w3}^6}{g^6 + c_{w3}^6}\right)^{\frac{1}{6}}, \quad g = r + c_{w2}(r^6 - r), \quad r = \frac{\mu \psi_{\mu_t^\star}}{\rho\, \hat{\omega}\, k^2\, d_{\min}^2}.$$

Note that with the definition (6), the source term tends to zero when $\mu_t^\star$ becomes negative. In [16], similar effects on the source term are obtained by directly setting to zero the source term for negative values of $\mu_t^\star$.

3. RD space discretization

In this section the RD space discretization of the steady Navier-Stokes equations is described. The numerical method used to discretize the system of equations follows from the scheme already proposed in [7] to discretize the scalar advection-diffusion problem and has subsequently been extended to discretization of the Navier-Stokes equations in [10].

The computational domain Ω is discretized with N_e non-overlapping elements with characteristic length h, the set of all the elements is denoted by $\mathcal{E}_h$, the list of the DOFs is denoted by $\mathcal{N}_h$, and the total number of DOFs is N_{dof}. The solution is approximated on each element by k-th order polynomials which are assumed to be continuous within the elements and on the faces of the elements. In this work Lagrangian basis functions are used to approximate the solution as follows

$$\mathsf{u}^h(\boldsymbol{x}) = \sum_{i \in \mathcal{N}_h} \psi_i(\boldsymbol{x})\, \mathsf{u}_i, \quad \boldsymbol{x} \in \Omega,$$

with u_i the numerical solution at the node, *i.e.*, degree of freedom (DOF), i and ψ_i the Lagrangian basis functions.

Due to the approximation of the solution, the integral of the Eq. (4) calculated on each element e will be not null, but it will give rise to a residual on each element, namely

$$\Phi^e(\mathsf{u}^h, \boldsymbol{\nabla}\mathsf{u}^h) = \int_{\Omega_e} \boldsymbol{\nabla}\cdot\left(\mathbf{f}^a(\mathsf{u}^h) - \mathbf{f}^v(\mathsf{u}^h, \boldsymbol{\nabla}\mathsf{u}^h)\right) \mathrm{d}\Omega + \int_{\Omega_e} \mathsf{S}(\mathsf{u}^h, \boldsymbol{\nabla}\mathsf{u}^h)\,\mathrm{d}\Omega, \tag{7}$$

where

$$\boldsymbol{\nabla}\mathsf{u}^h|_e = \sum_{i\in\mathcal{N}_h^e} \boldsymbol{\nabla}\psi_i\,\mathsf{u}_i,$$

is the internal gradient of the element e, computed with the gradient of the basis functions as in the Finite Element approach, and $\mathcal{N}_h^e$ is the set of DOFs of the element e. The integral quantity $\Phi^e(\mathsf{u}^h, \boldsymbol{\nabla}\mathsf{u}^h)$ is called total residual of the element e.

By using the divergence theorem, the first integral in Eq. (7) can be expressed as a surface integral and the divergence of the flux function is no longer required. This procedure is legitimate for the divergence of the advective flux, since the numerical solution by definition is continuous across the face of two neighbor elements. However, in handling the divergence of the viscous flux one has to cope with the fact that the normal component of internal gradient of the numerical solution is discontinuous across the face of two adjacent elements. The continuity of the normal flux across the element boundary is also necessary to show the consistency of the numerical scheme with respect to the original governing equations [17].

Suppose that $[\widetilde{\boldsymbol{\nabla}\mathsf{u}_i}]_{i=1,\dots,N_{\mathrm{dof}}}$ is the set of unique values of the gradient of the numerical solution, reconstructed at each DOF. The gradient can be now interpolated with the same basis functions used for the solution, namely

$$\widetilde{\boldsymbol{\nabla}\mathsf{u}^h}(\boldsymbol{x}) = \sum_{i\in\mathcal{N}_h} \psi_i(\boldsymbol{x})\,\widetilde{\boldsymbol{\nabla}\mathsf{u}_i}, \quad \boldsymbol{x}\in\Omega.$$

The quantity $\widetilde{\boldsymbol{\nabla}\mathsf{u}^h}$ is now continuous on the faces of the elements and the total residual can be written as follows

$$\begin{aligned}\Phi^e &= \oint_{\partial\Omega_e} \left(\mathbf{f}^a(\mathsf{u}^h) - \mathbf{f}^v(\mathsf{u}^h, \widetilde{\boldsymbol{\nabla}\mathsf{u}^h})\right)\cdot\boldsymbol{n}\,\mathrm{d}\partial\Omega + \int_{\Omega_e} \mathsf{S}(\mathsf{u}^h, \widetilde{\boldsymbol{\nabla}\mathsf{u}^h})\,\mathrm{d}\Omega,\\ &= \oint_{\partial\Omega_e} \left(\mathbf{f}^a(\mathsf{u}^h) - \mathbb{K}(\mathsf{u}^h)\widetilde{\boldsymbol{\nabla}\mathsf{u}^h}\right)\cdot\boldsymbol{n}\,\mathrm{d}\partial\Omega + \int_{\Omega_e} \mathsf{S}(\mathsf{u}^h, \widetilde{\boldsymbol{\nabla}\mathsf{u}^h})\,\mathrm{d}\Omega.\end{aligned} \tag{8}$$

Note that the reconstructed gradient has been used also in the definition of the source term. This term could be computed also with the internal gradient, but the reconstructed gradient is used for sake of accuracy and robustness. The procedure to recovery the gradient at each DOF, *i.e.*, how to compute $[\widetilde{\boldsymbol{\nabla}\mathsf{u}_i}]_{i=1,\dots,N_{\mathrm{dof}}}$, is detailed in Section 4.

Note that the idea to use a recovery procedure to remove the discontinuities at the element interfaces has been also used in the contest of DG methods for solving viscous flow problems [18, 19]. In these works, starting from the piece-wise discontinuous solution, a continuous approximation of the solution at the cell interface is reconstructed on the union of adjacent cells to the interface, and such continuous solution is used to evaluate the viscous flux function at the element interface.

In order to handle only nodal values, the total residual (8) is first distributed, in some way, to the DOFs of the element as follows

$$\Phi_i^e = \beta_i^e(\mathsf{u}^h)\,\Phi^e(\mathsf{u}^h, \widetilde{\boldsymbol{\nabla}\mathsf{u}^h}), \quad \forall i\in\mathcal{N}_h^e, \tag{9}$$

where β_i^e are the distribution coefficients, which can be in general function of u^h. It is easy to see that the nodal residuals, Φ_i^e, must satisfy the following conservation constrain [17]

$$\sum_{i\in\mathcal{N}_h^e} \Phi_i^e = \Phi^e, \quad \forall e\in\mathcal{E}_h. \tag{10}$$

Following [17], formal accuracy is achieved when, for a smooth exact solution $\mathsf{u}_{\mathrm{exact}}$ which is interpolated by u^h, the residuals Φ_i^e evaluated for that particular function satisfy

$$\Phi_i^e(\mathsf{u}^h) = O(h^{k+N_{\mathrm{dim}}}),$$

where N_{dim} is the geometrical dimension ($N_{\text{dim}} = 2, 3$) and k is the polynomial degree used to interpolate the solution. The form (9) satisfies this constraint, provided that the coefficients β_i^e are uniformly bounded with respect to the numerical solution and the mesh. If a set of residuals satisfies (9), then the scheme is said to be linearity preserving.

To obtain an equation for each nodal value of the numerical solution, the following relations are written for each DOF

$$\sum_{e \in \mathcal{E}_h^i} \Phi_i^e = 0, \quad \forall i \in \mathcal{N}_h, \tag{11}$$

where $\mathcal{E}_h^i$ is the set of the elements which share the DOF i. The previous relations define a set of non-linear equations that must be solved for the nodal values of the solution $[\mathsf{u}_i]_{i=1,\dots,N_{\text{dof}}}$. In practice, the solution with a RD method is obtained by the means of an iterative method, which in the simplest form reads

$$\frac{\mathsf{u}_i^{n+1} - \mathsf{u}_i^n}{\Delta t_i^n} = -\sum_{e \in \mathcal{E}_h^i} \Phi_i^e, \quad \forall i \in \mathcal{N}_h,$$

with Δt_i^n a scaled pseudo-time step. The change of the nodal values of the solution during the iterative process is driven by the non-zero total residuals on the elements; for $n \to \infty$ the total residual on each element vanishes and the steady state solution is obtained.

3.1. Construction of distribution schemes for advection-diffusion problems

The distribution process in Eq. (9) has been expressed through the use of generic distribution coefficients, the focus now is on how to actually construct a distribution scheme for the RANS equations. In this work, the attention is focused on the construction of centered schemes. Linear and non-linear schemes are considered.

3.1.1. Linear scheme

Consider a numerical scheme composed by an isotropic distribution plus a streamline term. This scheme has been successfully used in the context of the RD schemes to discretize the scalar advection-diffusion equation [7] and the Navier-Stokes equations [10]. The nodal residual, for a generic DOF i of the element e, can be written as follows

$$\Phi_i^e = \frac{\Phi^e}{N_{\text{dof}}^e} + \int_{\Omega_e} \mathbf{A} \cdot \boldsymbol{\nabla} \psi_i \, \Xi \left(\mathbf{A} \cdot \boldsymbol{\nabla} \mathsf{u}^h - \boldsymbol{\nabla} \cdot \left(\mathbb{K} \widetilde{\boldsymbol{\nabla} \mathsf{u}^h} \right) + \mathsf{S} \right) \mathrm{d}\Omega, \tag{12}$$

where N_{dof}^e is the number of DOFs of the element e, $\mathbf{A} = \partial \mathbf{f}^a / \partial \, \mathsf{u}$ is the inviscid flux Jacobian, and Ξ is a scaling matrix which is taken as

$$\Xi = \frac{1}{N_{\text{dim}}} |\Omega_e| \left(\sum_{i=1}^{N_{\text{dof}}^e} \mathsf{R}_{n_i}(\bar{\mathsf{u}}) \, \Lambda_{n_i}^+(\bar{\mathsf{u}}) \, \mathsf{L}_{n_i}(\bar{\mathsf{u}}) + \sum_{j=1}^{N_{\text{dim}}} \mathsf{K}_{jj}(\bar{\mathsf{u}}) \right)^{-1}, \tag{13}$$

where $\bar{\mathsf{u}}$ is the arithmetic average of the vector of the conservative variables on the element, R_n, L_n are respectively the matrices of the right and left eigenvectors along the direction of the vector $\boldsymbol{n}$, and $\Lambda_n = \mathrm{diag}(\lambda_n)$ is the corresponding diagonal matrix of the eigenvalues. The operator $(\cdot)^+$ selects only the positive values and sets the negative ones to zero. The vector $\boldsymbol{n}_i$ is taken as follows

$$\boldsymbol{n}_i = \frac{1}{N_{\text{dim}}} \int_{\Omega_e} \boldsymbol{\nabla} \psi_i \, \mathrm{d}\Omega,$$

such that it has the dimensions of a length (surface) in two (three) spatial dimensions.

The scheme is consistent since it achieves the conservation constraint (10). Formal accuracy is satisfied too: when the exact solution is injected in Eq. (13), the residual is zero because the total residual vanishes, and the integral term vanishes as well due to the fact that the terms in the integral at the right of the scaling matrix represent the governing equations.

The scheme is linearity preserving but not positive, which means that it is not guaranteed that it is monotone for discontinuous solutions. Due to the integral formulation, the scheme is valid for any type of element and for any order of approximation of the solution.

3.1.2. Non-linear scheme

Non-linear schemes are needed to combine the non-oscillatory behavior with the higher-order discretization. The basic idea to construct a non-linear scheme is to start with a first-order, monotone scheme, and to map its nodal residuals onto a set of positive and non-linear residuals [6]. To see in practice how to construct a non-linear scheme, consider the first order accurate and positive Rusanov's scheme (also know as the local Lax-Friedrichs scheme) defined as

$$\tilde{\Phi}_i^e = \frac{\Phi^e}{N_{\text{dof}}^e} + \frac{1}{N_{\text{dof}}^e}\,\alpha^e \sum_{\substack{j\in\mathcal{N}_h^e \\ j\neq i}} (\mathsf{u}_i - \mathsf{u}_j), \qquad \forall i \in \mathcal{N}_h^e,$$

with α^e large enough for stability, in practice it is taken as

$$\alpha^e = \max_{j\in\mathcal{N}_h^e}\left(|\lambda_{n_j}| + \left(\frac{\mu+\mu_t}{\rho} + \frac{\kappa+\kappa_t}{c_v}\right)_j\right).$$

Since the Rusanov's scheme is first-order accurate, its distribution coefficients, β_i^e, are unbounded. The construction of the non-linear scheme consists in mapping the distribution coefficients of the low order scheme onto non-linear bounded distribution coefficients As described in [6], the mapping for a system of equations is constructed in the characteristic space, consequently the nodal and the total residuals are first rewritten as

$$\Phi_i^{e\star} = \mathsf{L}_n \tilde{\Phi}_i^e \qquad \text{and} \qquad \Phi^{e\star} = \sum_{i\in\mathcal{N}_h^e} \Phi_i^{e\star},$$

where the mean fluid velocity vector on the element is used as direction vector to compute the eigenvectors. The nodal high-order residuals are obtained as follows

$$\hat{\Phi}_i^{e\star} = \hat{\beta}_i^{e\star}\Phi^{e\star},$$

with the bounded distribution coefficients, $\hat{\beta}_i^{e\star}$, obtained by applying a non-linear mapping to the original unbounded distribution coefficients, $\beta_i^{e\star} = \Phi_i^{e\star}/\Phi^{e\star}$. The map is constructed as follows

$$\hat{\beta}_i^{e\star} = \frac{\left(\dfrac{\Phi_i^{e\star}}{\Phi^{e\star}}\right)^+}{\displaystyle\sum_{j\in\mathcal{N}_h^e}\left(\frac{\Phi_i^{e\star}}{\Phi^{e\star}}\right)^+},$$

which correspond to the so-called PSI limiter. Finally, the high-order nodal residuals are projected back on the physical space: $\hat{\Phi}_i^e = \mathsf{R}_n\hat{\Phi}_i^{e\star}$.

The use of a centered scheme, like the Rusanov's scheme, in combination with the limiting technique, produces undamped spurious modes and a poor iterative convergence to the steady state solution [6] due to the fact that no upwind mechanism is included. The cure to this problem consists in adding a filtering term by means of a streamline dissipation term

$$\Phi_i^e = \hat{\Phi}_i^e + \varepsilon_h^e(\mathsf{u}^h)\int_{\Omega_e}\Big(\mathbf{A}\cdot\boldsymbol{\nabla}\psi_i - \boldsymbol{\nabla}\cdot(\mathbb{K}\boldsymbol{\nabla}\psi_i)\Big)\,\Xi\Big(\mathbf{A}\cdot\boldsymbol{\nabla}\mathsf{u}^h - \boldsymbol{\nabla}\cdot(\mathbb{K}\widetilde{\boldsymbol{\nabla}\mathsf{u}^h}) + \mathsf{S}\Big)\,\mathrm{d}\Omega. \tag{14}$$

where the scaling matrix Ξ is defined as in Eq. (13). The term $\varepsilon_h^e(\mathsf{u}^h)$ is a smoothness sensor which assures that the filtering term is added only in the smooth regions of the solution, namely $\varepsilon_h^e(\mathsf{u}^h) \sim 1$ in smooth regions and $\varepsilon_h^e(\mathsf{u}^h) \sim 0$ near discontinuities. A pressure-based shock sensor is used for $\varepsilon_h^e(\mathsf{u}_h)$, see [20],

$$\varepsilon_h^e(\mathsf{u}_h) = 1 - \max_{i\in\mathcal{N}_h^e}\left(\max_{e\in\mathcal{E}_h^i}\left(\frac{|P_i - \bar{P}_e|}{|P_i| + |\bar{P}_e| + \epsilon}\right)\right),$$

where P_i is the pressure at the DOF i, $\bar{P}_e$ is the arithmetic average of the pressure on the element e, and $\epsilon = 10^{-12}$.

3.2. Improved discretization of the diffusion terms

The schemes (12) and (14) might have a high numerical error. Following the previous works [7, 10], in order to improve in the numerical schemes suppose to write the governing system of equations in the following form

$$\begin{cases} \boldsymbol{\nabla}\cdot\mathbf{f}^a(\mathsf{u}) - \boldsymbol{\nabla}\cdot(\mathbb{K}\mathsf{w}) = 0 \\ \mathsf{w} - \boldsymbol{\nabla}\mathsf{u} = 0 \end{cases} \tag{15}$$

where for sake of simplicity the source term has been omitted, since it is irrelevant to the analysis. In the previous system, the additional variable w has been introduced for the gradients, in this way the original second order governing equations can be recasted as a first order system. The first order formulation for viscous problems has become a very standard approach in the DG framework, where numerical fluxes for the solution, u, and the gradient variable, w, are introduced to handle the discontinuities at interface of the elements [21]. Here, the discontinuity of the variable w at the faces of the elements is taken into account via the gradient reconstruction procedure.

Consider a numerical scheme for the system (15) composed by a centered contribution plus a streamline stabilization term, namely

$$\int_{\Omega_e} \psi_i \begin{pmatrix} \boldsymbol{\nabla}\cdot\mathbf{f}^a(\mathsf{u}^h) - \boldsymbol{\nabla}\cdot(\mathbb{K}\mathsf{w}) \\ \mathsf{w} - \boldsymbol{\nabla}\mathsf{u}^h \end{pmatrix} \mathrm{d}\Omega + \int_{\Omega_e} \mathbb{A}\cdot\boldsymbol{\nabla}\psi_i \, \mathbb{T} \begin{pmatrix} \boldsymbol{\nabla}\cdot\mathbf{f}^a(\mathsf{u}^h) - \boldsymbol{\nabla}\cdot(\mathbb{K}\mathsf{w}) \\ \mathsf{w} - \boldsymbol{\nabla}\mathsf{u}^h \end{pmatrix} \mathrm{d}\Omega = 0, \tag{16}$$

where

$$\mathbb{A}\cdot\boldsymbol{\nabla}\psi_i = \begin{pmatrix} \mathbf{A}\cdot\boldsymbol{\nabla}\psi_i & -\mathbb{K}\cdot\boldsymbol{\nabla}\psi_i \\ -\boldsymbol{\nabla}\psi_i & 0 \end{pmatrix},$$

and the scaling term is taken as follows

$$\mathbb{T} = \begin{pmatrix} \Xi & 0 \\ 0 & \Xi_d \end{pmatrix}.$$

Supposing, now, that the gradient of the numerical solution has been reconstructed at each DOF, one can replace the equation on the second line of the system (16) with the approximation $\mathsf{w} \simeq \widetilde{\boldsymbol{\nabla}\mathsf{u}^h}$ and consider only the first line, which now reads

$$\begin{aligned} \int_{\Omega_e} \psi_i \left(\boldsymbol{\nabla}\cdot\mathbf{f}^a(\mathsf{u}^h) - \boldsymbol{\nabla}\cdot(\mathbb{K}\widetilde{\boldsymbol{\nabla}\mathsf{u}^h})\right)\mathrm{d}\Omega \; + \int_{\Omega_e} \mathbf{A}\cdot\boldsymbol{\nabla}\psi_i \, \Xi\left(\mathbf{A}\cdot\boldsymbol{\nabla}\mathsf{u}^h - \boldsymbol{\nabla}\cdot\left(\mathbb{K}\widetilde{\boldsymbol{\nabla}\mathsf{u}^h}\right)\right)\mathrm{d}\Omega \\ + \int_{\Omega_e} \mathbb{K}\,\boldsymbol{\nabla}\psi_i \cdot \left(\Xi_d\left(\boldsymbol{\nabla}\mathsf{u}^h - \widetilde{\boldsymbol{\nabla}\mathsf{u}^h}\right)\right)\mathrm{d}\Omega = 0. \end{aligned} \tag{17}$$

The first two integrals in the previous equation represent the discretization for the advection-diffusion problem by the means of a centered scheme plus a streamline stabilization term. The last integral represents an additional stabilization term, for the diffusive terms only, which vanishes in the advective limit, and the parameter matrix Ξ_d is dimensionless. It is interesting to note that the role of this additional term is to penalize the difference between the discontinuous and the reconstructed gradients, on each element. As already observed in the case of the Navier-Stokes equations [10], taking Ξ_d as the identity matrix is a good choice. Further studies on the effect of Ξ_d on the numerical scheme are left for future work.

With the Eq. (17) in mind, the schemes (12) and (14) are modified in order to include the extra stabilization term for the diffusive part of the equation. Namely, the linear scheme reads

$$\begin{aligned} \Phi_i^e = \frac{\Phi^e}{N_{\mathrm{dof}}^e} \; + \int_{\Omega_e} \mathbf{A}\cdot\boldsymbol{\nabla}\psi_i \, \Xi\left(\mathbf{A}\cdot\boldsymbol{\nabla}\mathsf{u}^h - \boldsymbol{\nabla}\cdot(\mathbb{K}\boldsymbol{\nabla}\mathsf{u}^h) + \mathsf{S}\right)\mathrm{d}\Omega \\ + \int_{\Omega_e} \mathbb{K}\,\boldsymbol{\nabla}\psi_i \cdot \left(\boldsymbol{\nabla}\mathsf{u}^h - \widetilde{\boldsymbol{\nabla}\mathsf{u}^h}\right)\mathrm{d}\Omega, \end{aligned} \tag{18}$$

while the non-linear scheme becomes

$$\begin{aligned} \Phi_i^e = \hat{\Phi}_i^e \; + \varepsilon_h^e(\mathsf{u}^h) \int_{\Omega_e} \left(\mathbf{A}\cdot\boldsymbol{\nabla}\psi_i - \boldsymbol{\nabla}\cdot(\mathbb{K}\boldsymbol{\nabla}\psi_i)\right)\Xi\left(\mathbf{A}\cdot\boldsymbol{\nabla}\mathsf{u}^h - \boldsymbol{\nabla}\cdot(\mathbb{K}\widetilde{\boldsymbol{\nabla}\mathsf{u}^h}) + \mathsf{S}\right)\mathrm{d}\Omega \\ + \int_{\Omega_e} \mathbb{K}\,\boldsymbol{\nabla}\psi_i \cdot \left(\boldsymbol{\nabla}\mathsf{u}^h - \widetilde{\boldsymbol{\nabla}\mathsf{u}^h}\right)\mathrm{d}\Omega. \end{aligned} \tag{19}$$

4. Gradient recovery strategies

As explained in Section 3, one has to assume that a continuous value of the gradient of the numerical solution is available on the faces of the elements. The strategy adopted here to achieve this goal consists in recovering the gradients at the DOFs, then the nodal values of the gradient are interpolated with Lagrangian basis functions. It is evident that the gradient reconstruction represents a key point to get higher-order accuracy. On the other hand, the computational effort in the gradient reconstruction should be as limited as possible.

In [7] different reconstruction strategies were considered, and it was found that the so-called Super-convergent Patch Recovery method proposed by Zienkiewicz and Zhu [8, 9] (SPR-ZZ) offers the possibility to reconstruct the gradients with the same order of accuracy of the solution, without spoiling the compactness of the numerical scheme. It was shown that the SPR-ZZ is much more accurate than other common approaches like Green-Gauss, L^2-projection or least-square, which fail to reconstruct the gradient with more than second-order of accuracy.

Furthermore, in [10] it is shown that if the gradient of the numerical solution is not reconstructed with same order of accuracy of the numerical solution, the overall accuracy of the numerical scheme is spoiled in regions where diffusive effects prevail over the advective ones or where advection and diffusion are equally important.

For sake of clarity Super-convergent Patch Recovery method is briefly recalled here.

4.1. Super-convergent Patch Recovery

The gradient of the numerical solution sampled at certain points on the element may have the same order of accuracy of the discrete solution [22]. It can be shown that in the case of a segment element such particular points correspond to the Gauss-Legendre points [23]. By tensor product such points can be defined also for quadrangles and hexahedrons. For triangles or tetrahedrons such property cannot be rigorously shown, but numerical experiments confirm it.

Using this fact, it is possible to compute a high-order accurate gradient within the whole element. Indeed, if at the super-convergent points the value of the gradient is accurate to order $k+1$, by using a polynomial of degree k (the same of the solution) it is possible to obtain a high-order approximation everywhere within the element if this polynomial fits the super-convergent gradient values in a least square manner within a patch of the elements. Such a technique is called super-convergent patch recovery, introduced by Zienkiewicz and Zhu (SPR-ZZ) [8, 9].

Consider, for simplicity, a two dimensional scalar problem and assume that u^h is the piecewise continuous polynomial interpolation of degree k of the solution u. The aim here is to reconstruct the gradient of the numerical solution at the DOFs, with $(k+1)$-th order of accuracy. For each vertex of the grid a patch is defined as the union of all the elements that share that vertex, see Fig. 2. On the patch, the components of the reconstructed gradient are written in a polynomial form as follows

$$\widetilde{\frac{\partial u^h}{\partial x}} = \boldsymbol{p}^{\mathrm{T}}\boldsymbol{a}_x, \quad \text{and} \quad \widetilde{\frac{\partial u^h}{\partial y}} = \boldsymbol{p}^{\mathrm{T}}\boldsymbol{a}_y, \tag{20}$$

with

$$\boldsymbol{p}^{\mathrm{T}}(\boldsymbol{x}) = (1, x, y, x^2, \ldots, x^k, x^{k-1}y, \ldots, y^k),$$
$$\boldsymbol{a}_x = (a_{x_1}, a_{x_2}, \ldots, a_{x_m}) \quad \text{and} \quad \boldsymbol{a}_y = (a_{y_1}, a_{y_2}, \ldots, a_{y_m}).$$

On each element of the patch the gradient of the numerical solution has the highest accuracy at the super-convergent points. Thus, the high-order accurate expression of the reconstructed gradient on the patch is obtained by a least square fitting of the polynomial expressions (20) to the values of the gradient at the super-convergent points of the patch.

Assuming that N_{s_i} super-convergent points, $\boldsymbol{x}_{i,\ell}, \ell = 1 \ldots N_{s_i}$, are available over the patch built around the vertex i, the values of the coefficients $\boldsymbol{a}_{x_i}$ and $\boldsymbol{a}_{y_i}$ are obtained by introducing the following functions

$$F_{x_i} = \sum_{k=1}^{N_{s_i}} \left(\frac{\partial u^h}{\partial x}(\boldsymbol{x}_{i,k}) - \boldsymbol{p}_{i,k}^{\mathrm{T}}\boldsymbol{a}_{x_i} \right)^2 \quad \text{and} \quad F_{y_i} = \sum_{k=1}^{N_{s_i}} \left(\frac{\partial u^h}{\partial y}(\boldsymbol{x}_{i,k}) - \boldsymbol{p}_{i,k}^{\mathrm{T}}\boldsymbol{a}_{y_i} \right)^2,$$

with $\boldsymbol{p}_{i,k} = \boldsymbol{p}(\boldsymbol{x}_{i,k})$, and by minimizing them with respect to the polynomial coefficients, that is

$$\frac{\partial F_{x_i}}{\partial \boldsymbol{a}_{x_i}} = 0 \quad \text{and} \quad \frac{\partial F_{y_i}}{\partial \boldsymbol{a}_{y_i}} = 0.$$

The minimization problem for the patch around the vertex i requires the solution of the following linear systems

$$A_i \boldsymbol{a}_{x_i} = \boldsymbol{b}^h_{x_i} \quad \text{and} \quad A_i \boldsymbol{a}_{y_i} = \boldsymbol{b}^h_{y_i}, \tag{21}$$

in a least-square sense, where

$$\boldsymbol{b}^h_{x_i} = \begin{pmatrix} \dfrac{\partial u^h}{\partial x}(\boldsymbol{x}_{i,1}) \\ \dfrac{\partial u^h}{\partial x}(\boldsymbol{x}_{i,2}) \\ \vdots \\ \dfrac{\partial u^h}{\partial x}(\boldsymbol{x}_{i,N_{s_i}}) \end{pmatrix}, \quad \boldsymbol{b}^h_{y_i} = \begin{pmatrix} \dfrac{\partial u^h}{\partial y}(\boldsymbol{x}_{i,1}) \\ \dfrac{\partial u^h}{\partial y}(\boldsymbol{x}_{i,2}) \\ \vdots \\ \dfrac{\partial u^h}{\partial y}(\boldsymbol{x}_{i,N_{s_i}}) \end{pmatrix} \quad \text{and} \quad A_i = \begin{pmatrix} 1 & x_{i,1} & y_{i,1} & \cdots & y^k_{i,1} \\ 1 & x_{i,2} & y_{i,2} & \cdots & y^k_{i,2} \\ \vdots & \vdots & \vdots & \ddots & \vdots \\ 1 & x_{i,N_{s_i}} & y_{i,N_{s_i}} & \cdots & y^k_{i,N_{s_i}} \end{pmatrix}.$$

Once the vectors $\boldsymbol{a}_{x_i}$ and $\boldsymbol{a}_{y_i}$ are known, the reconstructed gradient $\widetilde{\boldsymbol{\nabla} u^h}$ can be evaluated at any point within the patch around the vertex i.

The dimensions of the matrix A_i are determined by the number of super-convergent points N_{s_i} and by the degree of the polynomials used to express the reconstructed gradient, that is $A_i \in \mathbb{R}^{N_{s_i} \times m}$, where m is the number of the coefficients in the vectors $\boldsymbol{a}_{x_i}$ and $\boldsymbol{a}_{y_i}$. The problem admits an unique solution if $\operatorname{Rank} A_i = m$, which is always satisfied in the case in which $N_{s_i} \geq m$. Note that the SPR-ZZ method requires only the solution of small linear systems instead of a single large system as that obtained by a global L^2 projection. Note that, since the matrices A_i depend only on the geometry, they are computed and factorized only once.

Generally, the number of elements contained in the patch is such that the condition $N_{s_i} \geq m$ is always satisfied, this means that the gradient reconstruction is compact because it involves only the elements contained within the support of a grid vertex.

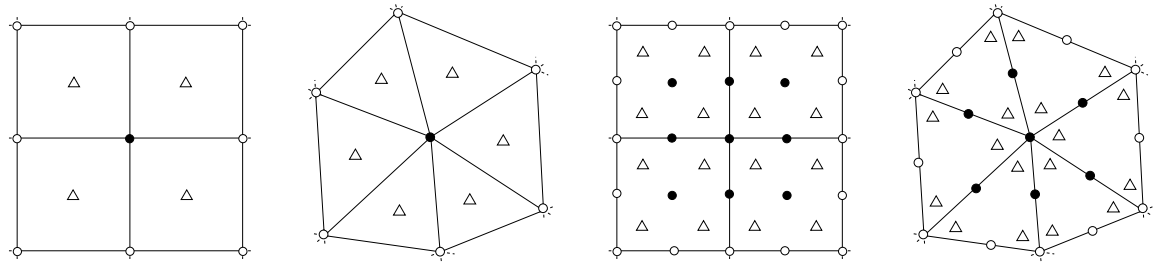

(a) (b) (c) (d)

Figure 2: Interior super-convergent patches for quadrilateral and triangular elements: (a-b) linear elements, (c-d) quadratic elements. The symbols (∘) indicate the patch assembly points, the symbols (•) indicate the points where the gradient is reconstructed and the symbols (△) indicate the super-convergent points.

It is important to remark that the SPR-ZZ method solves for the vector of the polynomial coefficients, $\boldsymbol{a}_x$ and $\boldsymbol{a}_y$ over each patch, instead of solving for the nodal values of the reconstructed gradient as in the classical least-square gradient reconstruction. Once the polynomial coefficients are computed on the patch associated to a grid vertex, they can be used to evaluate the gradient at any point on that patch. As matter of fact, for the extra nodes introduced by the higher order approximation of the solution, the gradient is reconstructed by simply evaluating on the patch, at the coordinates of the nodes, the polynomial function constructed for the nearest grid vertex. Note that these nodes may belong to more than one patch, each of them is equally valid to evaluate the gradient. An arithmetic average is used to uniquely define the reconstructed gradient at these nodes.

The same idea is used to get the value of the reconstructed gradient at the boundary of the domain. In fact, for the nodes belonging to the boundary, the condition $N_{s_i} \geq m$ might not be satisfied without enlarging the stencil. To avoid the use of larger stencils for boundary nodes, it is possible to obtain the value of the reconstructed gradient at

the boundary by evaluating, at the boundary node, the polynomial expansion already computed for the nearest domain vertex, *i.e.*, the interior patch is used to evaluate the gradient at the boundary.

Another advantage of the SPR-ZZ approach is that being based on an element-wise evaluation (the super-convergent points inside the element of the patch where the gradient is evaluated), the stencil of the SPR-ZZ method is smaller than that required by the direct used of the least-square gradient reconstruction method, which is based on a nodal evaluation of the solution. In fact, it was observed in [7] that if the stencil used for the gradient reconstruction is made only by the nearest neighbor elements, the least square gradient reconstruction is at the most second order accurate.

For a quadrangle, the super-convergent points are defined uniquely. Considering a reference segment defined as $x = [-1, 1]$, the super-convergent point is the point $x = 0$ in the case of a linear element, while in the case of a quadratic element the super-convergent points have coordinates $\pm 1/\sqrt{3}$. The super-convergent points on the reference quadrangle are simply obtained by a tensorial product of the points defined on the reference segment.

For a linear triangle, the super-convergent point is the point with barycentric coordinates $\boldsymbol{\lambda} = (1/3, 1/3, 1/3)$, while in the case of a quadratic triangle the super-convergent points are not unique. In [7], it was shown that the following choice of the super-convergent points coordinates

$$\boldsymbol{\lambda}_1 = \left(\frac{2}{3}, \frac{1}{3}, \frac{1}{3}\right), \quad \boldsymbol{\lambda}_2 = \left(\frac{1}{3}, \frac{2}{3}, \frac{1}{3}\right), \quad \text{and} \quad \boldsymbol{\lambda}_3 = \left(\frac{1}{3}, \frac{1}{3}, \frac{2}{3}\right).$$

is optimal, where $\boldsymbol{\lambda}_{1,2,3}$ are the coordinates of the super-convergent points in the barycentric coordinate system.

5. Non-Linear LU-SGS Implicit Solver

The RANS equations are generally stiffer than the Navier-Stokes equations, in addition, since in turbulent flows the variation of the solution in the direction normal to wall is much higher than that in the tangential direction, very stretched grids are usually used in numerical simulations of turbulent flows. These factors, makes the solution of turbulent problems much more difficult than laminar ones and the robustness of the numerical solver is drastically reduced.

In [10], a matrix-free approach with the LU-SGS preconditioner was developed for the Navier-Stokes equations, showing very good performance in the simulation of laminar flows. Later, in this work it has been observed that the robustness and the effectiveness of the matrix-free solver are drastically reduced in the simulation of turbulent flows. In fact, this approach usually fails with a sudden breakdown of the solver or it stagnates at high values of the residual.

Since high-order methods are generally less robust than standard low-order methods the construction of a reliable implicit solver becomes crucial. For these reasons, instead of using a matrix-free based Newton-Krylov method a different strategy has been adopted for the solution of the non-linear system obtained from the discretization of the RANS equations.

Consider the solution of the non-linear system Eq. (11) with the Newton's scheme, which is written as

$$\left(\frac{\mathbb{I}}{\Delta t^n} + \frac{\partial \mathbf{R}}{\partial \mathsf{u}}\right)\Delta \mathsf{u}_h^n = -\mathbf{R}(\mathsf{u}_h^n), \tag{22}$$

where $\mathbf{R}(\mathsf{u}_h^n)$ is the spatial residual of the numerical scheme at the time level n. The previous equation can be recasted in the following form

$$\left(\frac{\mathbb{I}}{\Delta t^n} + \frac{\partial \mathbf{R}_i}{\partial \mathsf{u}_i}\right)\Delta \mathsf{u}_i^n = -\mathbf{R}_i(\mathsf{u}^n) - \sum_{\substack{j \in \mathcal{N}_h^i \\ j \neq i}} \frac{\partial \mathbf{R}_i}{\partial \mathsf{u}_j}\Delta \mathsf{u}_j^n, \quad \forall\, i \in \mathcal{N}_h, \tag{23}$$

where $\mathcal{N}_h^i$ is the set of the DOFs contained in the stencil of DOF i. When the Gauss-Seidel method is applied to solve (23), the forward and backward sweep steps read

$$\left(\frac{\mathbb{I}}{\Delta t^n} + \frac{\partial \mathbf{R}_i}{\partial \mathsf{u}_i}\right)\Delta \mathsf{u}_i^* = -\mathbf{R}_i(\mathsf{u}^n) - \sum_{\substack{j \in \mathcal{N}_h^i \\ j < i}} \frac{\partial \mathbf{R}_i}{\partial \mathsf{u}_j}\Delta \mathsf{u}_j^*, \quad i = 1, 2, \ldots, N_{\text{dof}},$$

$$\left(\frac{\mathbb{I}}{\Delta t^n}+\frac{\partial \mathbf{R}_i}{\partial \mathsf{u}_i}\right)(\Delta \mathsf{u}_i^n-\Delta \mathsf{u}_i^*)=-\sum_{\substack{j\in\mathcal{N}_h^i\\ j>i}}\frac{\partial \mathbf{R}_i}{\partial \mathsf{u}_j}\Delta \mathsf{u}_j^n,\quad i=N_{\text{dof}},\ldots,2,1.$$

A better scheme can be obtained by applying a symmetric variation of the Gauss-Seidel method, in which both forward and backward steps are applied alternatively. The forward and backward sweep steps can be written in concise form as

$$\left(\frac{\mathbb{I}}{\Delta t^n}+\frac{\partial \mathbf{R}_i}{\partial \mathsf{u}_i}\right)\Delta \mathsf{u}_i^{(k+1)}=-\mathbf{R}_i(\mathsf{u}^n)-\sum_{\substack{j\in\mathcal{N}_h^i\\ j\neq i}}\frac{\partial \mathbf{R}_i}{\partial \mathsf{u}_j}\Delta \mathsf{u}_j^{(*)},\quad \forall\, i\in\mathcal{N}_h, \tag{24}$$

where k is an inner iteration index, the superscript $^{(*)}$ indicates the most recently updated solution, and $\Delta \mathsf{u}^{(0)}=0$. At the end, $\mathsf{u}^{n+1}=\mathsf{u}^n+\Delta \mathsf{u}^{(k+1)}$.

The right-hand side of the previous equation can be further manipulated as follows. Denoting the latest available solution as $\mathsf{u}^{(*)}=\mathsf{u}^n+\Delta \mathsf{u}^{(*)}$, it is possible to linearize $\mathbf{R}_i(\mathsf{u}^{(*)})$ as

$$\begin{aligned}\mathbf{R}_i(\mathsf{u}^{(*)})&\approx \mathbf{R}_i(\mathsf{u}^n)+\sum_{j\in\mathcal{N}_h^i}\frac{\partial \mathbf{R}_i}{\partial \mathsf{u}_j}\Delta \mathsf{u}_j^{(*)}\\ &=\mathbf{R}_i(\mathsf{u}^n)+\frac{\partial \mathbf{R}_i}{\partial \mathsf{u}_i}\Delta \mathsf{u}_i^{(*)}+\sum_{\substack{j\in\mathcal{N}_h^i\\ j\neq i}}\frac{\partial \mathbf{R}_i}{\partial \mathsf{u}_j}\Delta \mathsf{u}_j^{(*)},\end{aligned}$$

and the following relation is obtained

$$\mathbf{R}_i(\mathsf{u}^n)+\sum_{\substack{j\in\mathcal{N}_h^i\\ j\neq i}}\frac{\partial \mathbf{R}_i}{\partial \mathsf{u}_j}\Delta \mathsf{u}_j^{(*)}=\mathbf{R}_i(\mathsf{u}^{(*)})-\frac{\partial \mathbf{R}_i}{\partial \mathsf{u}_i}\Delta \mathsf{u}_i^{(*)}.$$

Substituting the previous relation in Eq. (24), one obtains the following scheme

$$\left[\frac{\mathbb{I}}{\Delta t^n}+\frac{\partial \mathbf{R}_i}{\partial \mathsf{u}_i}\right]\Delta \mathsf{u}_i^{(k+1)}-\frac{\partial \mathbf{R}_i}{\partial \mathsf{u}_i}\Delta \mathsf{u}_i^{(*)}=-\mathbf{R}_i(\mathsf{u}^{(*)}),$$

which at last can be recasted as

$$\left[\frac{\mathbb{I}}{\Delta t^n}+\frac{\partial \mathbf{R}_i}{\partial \mathsf{u}_i}\right]\left(\Delta \mathsf{u}_i^{(k+1)}-\Delta \mathsf{u}_i^{(*)}\right)=-\mathbf{R}_i(\mathsf{u}^{(*)})+\frac{\Delta \mathsf{u}_i^{(*)}}{\Delta t^n}. \tag{25}$$

The Eq. (25) is solved with the forward and backward sweeps. At the beginning of each step the small diagonal blocks of the Jacobian matrix in the left-hand side can be inverted using the LU decomposition. The last term in the right hand side of the (25) is usually dropped for steady simulations, in order to accelerate the convergence rate. Note that the right-hand side of the previous equation is nothing but the residual evaluated with the latest available solution. When the symmetric Gauss-Seidel converges, one is actually solving the original set of equations instead of the linearized version (22), for this reason the algorithm is called non-linear LU-SGS [24].

The expression (25) only requires the diagonal blocks of the Jacobian matrix. In some works [24, 25, 26] the diagonal blocks of the Jacobian are approximated with a finite difference method, however this strategy has been found unsatisfactory for RANS simulations, thus the approximated diagonal blocks are computed directly.

The evolution of time step Δt^n used to dampen the solution, is controlled by the CFL number that is chosen according to the following law [27]

$$\text{CFL}^n=\text{CFL}^{n-1}\frac{\|\mathbf{R}(\mathsf{u}^{n-2})\|_\infty}{\|\mathbf{R}(\mathsf{u}^{n-1})\|_\infty},$$

starting from a low CFL number, typically $\text{CFL}^0=1$ and limiting the maximum value of the CFL to $\text{CFL}_{\max}=1\,000$. The iterative process is stopped when the residual of the equations becomes small enough with respect to the initial value.

6. Numerical Results

The linear and non-linear RD schemes previously described are now used to perform numerical simulations of subsonic and transonic turbulent flows.

In all the simulations, on the wall hybrid weak-strong boundary conditions are applied: the velocity ($\boldsymbol{v} = 0$) and the turbulent working variable ($\mu_t^\star = 0$) are strongly imposed on the wall, while the adiabatic condition is weakly enforced. The in/out-flow, far-field boundary and symmetric conditions are imposed in a weak way. The procedure used to impose the boundary conditions in the RD framework is detailed in previous works [28, 10].

6.1. High Reynolds Number Flow over a Flat Plate

The two dimensional turbulent flow over a flat plate is here considered. The free-stream Mach number is M = 0.2 and the Reynolds number, computed with the free-stream conditions and an unity length of the plate, is $\mathrm{Re} = 5 \times 10^6$, and the length of the plate is L = 2. The range of the computational domain in the x-direction is $[-0.33, 2]$ with the leading edge of the flat plate at $x = 0$. The size of the computational domain in the y-direction is 1, which is about 66 times the boundary layer thickness at $x = 2$. At the inlet, the inflow boundary condition is imposed, while at the top and the exit, the static pressure is imposed. Along the plane $y = 0$, the symmetry boundary condition is imposed for $-0.33 \leq x \leq 0$ and the adiabatic no-slip wall boundary condition is imposed for $0 \leq x \leq 2$. The free-stream value of the turbulent working variable is such that $\mu_t^\star / \mu_\infty = 3$.

A sequence of uniformly refined grids is considered. The coarsest grid is obtained by the triangulation of a 35×25 structured grid; the first number refers to the number of nodes on the horizontal boundaries, with 29 nodes along the plate, the second number refers to the number of nodes on the vertical boundaries. The grid is stretched in the wall-normal direction, and is also clustered near the plate leading edge; the height of the elements along the wall is 8.32×10^{-6}. Finer grids are obtained by applying successive uniform refinements to the coarsest grid.

Except for the singularity of the solution at the leading edge of the plate, the flow is smooth and for this reason the linear scheme is used. For each grid, simulations with linear and quadratic approximation of the solution are performed, and the L^2 norms of the residuals of the mean flow and turbulence equations are reduced by ten orders of magnitude.

The skin friction distributions along the plate with linear and quadratic approximation of the solution, for grids with different resolutions, are reported in Fig. 3 as function of the quantity $\mathrm{Re}_x = x\|\boldsymbol{v}_\infty\|/\mu_\infty$. For reference, the experimental measures of Wieghardt [29] are also reported.

Note that the linear approximation of the solution gives a quite poor resolution of the friction coefficient along the plate and the solution is still far from a grid independent value, even for the finest grid. The quadratic approximation of the solution, on the other hand, gives very regular profiles of the friction coefficient. The values agree well with the experimental data and it is also clear that a reasonable accurate solution is already obtained on the coarsest mesh.

A quantitative comparison between the linear and quadratic approximations of the solution is reported in Fig. 4-a, where the values of the drag coefficient are reported as function of the number of DOFs. A reference value of the drag coefficient was obtained with a Richardson extrapolation [30] of the drag coefficients computed with quadratic elements.

It is evident how, for the same number of degrees of freedom, the solution computed with the quadratic elements converges faster to the reference value, than the solution computed with the linear approximation. Thus, a second order scheme requires much more DOFs than the third order scheme to get a grid independent and accurate solution. This can be observed also in figure Fig. 4-b, where the error for the drag coefficient is reported as function of the number of the degrees of freedom. The error is computed as the absolute value of the difference between the numerical value of the drag coefficient and the reference one, *i.e.*, $err_{\mathrm{CD}} = |c_{D_h} - c_{D_{\mathrm{ref}}}|$.

In Fig. 5 are also reported the profiles of the axial velocity in the boundary layer at the station $x = 0.97$, in terms of dimensionless quantities. The dimensionless distance from the plate is defined as $y^+ = y\rho u_\tau/\mu$, with the friction velocity given by $u_\tau = \sqrt{\left(\mu \frac{\partial v_x}{\partial y}\right)\Big|_{\mathrm{wall}}}$, the dimensionless velocity is defined as $u^+ = v_x/u_\tau$. The figures report also the law-of-wall profiles computed according to the following equations [31]

$$\begin{cases} u^+ = y^+, & \text{in the viscous sublayer} \\ u^+ = \dfrac{1}{\kappa} \log y^+ + B, & \text{in the loglayer} \end{cases} \tag{26}$$

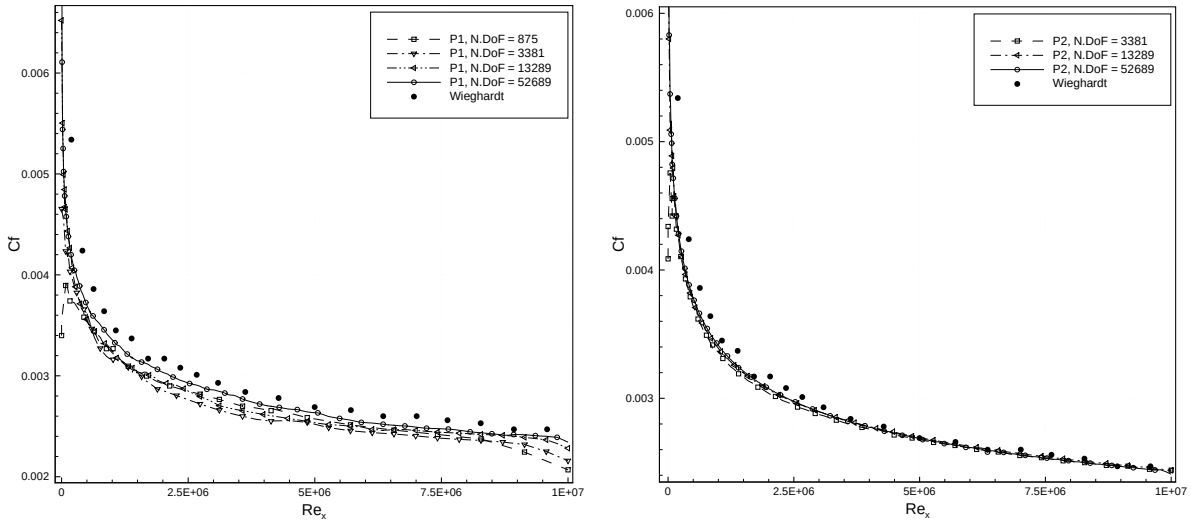

(a) (b)

Figure 3: Friction coefficient along the plate for the turbulent flow over a flat plate, with different grid resolutions and with linear (a) and quadratic (b) approximation of the solution.

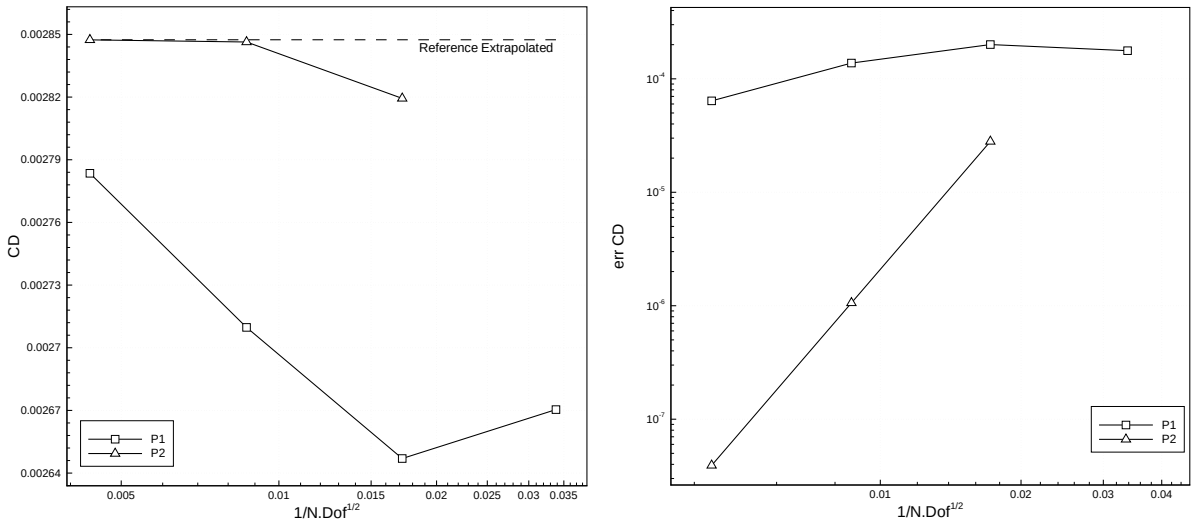

(a) (b)

Figure 4: Effects of the grid and polynomial refinement on the solution accuracy for the turbulent flow over a flat plate: (a) drag coefficients (b) error on the computation of the drag coefficient.

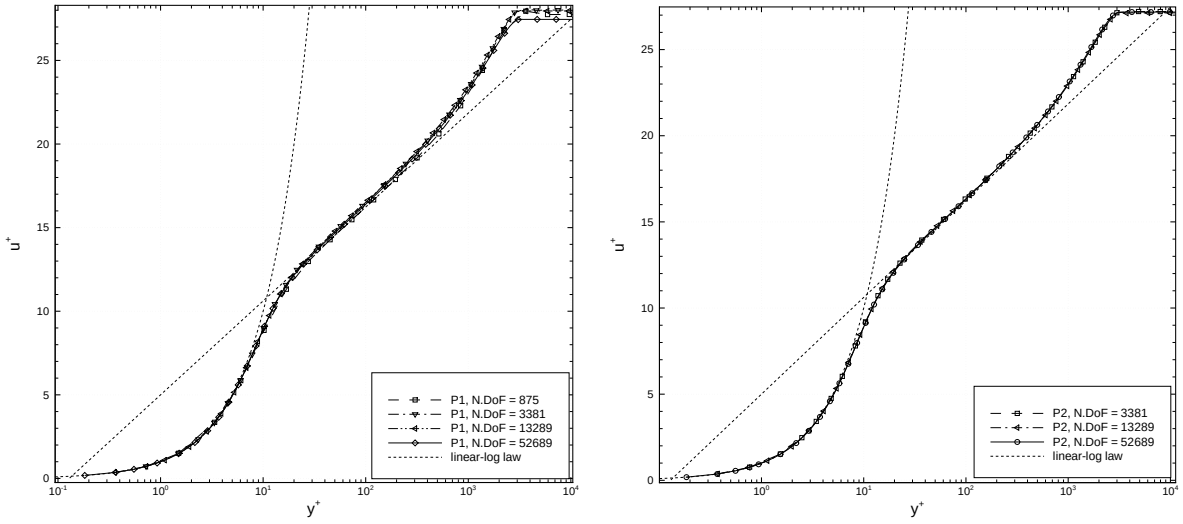

(a) (b)

Figure 5: Dimensionless axial velocity profiles in the boundary layer at the point $x = 0.97$ for the turbulent flow over a flat plate, with different grid resolutions and with linear (a) and quadratic (b) approximation of the solution.

where $\kappa = 0.41$ is the von Karman constant and $B = 5$. Note that, since the friction velocity is based on the computed skin friction values at the wall, the dimensionless quantities depend on the accuracy of the solution. For linear approximation of the solutions, a good agreement with the theoretical profiles in the viscous sub-layer and in the log-layer regions is obtained. Also in the outer part of the boundary layer the velocity profiles dependent only a little on the grid resolution. Differences in the velocity profiles for quadratic elements can hardly be observed from the figure.

In Fig. 6 are reported the profiles of the quantity $\chi = \mu_t^\star / \mu$ at the station $x = 0.97$, to show the turbulent working variable along the boundary layer. Note that when the spatial resolution is poor (generally at the outer part of the boundary layer) negative values of the turbulent working variable might be obtained, however this effect is canceled out with the mesh refinement and/or the order increment of the numerical discretization.

6.2. Subsonic Flow over a RAE2822 Airfoil

The second test case considered is the subsonic flow over a RAE2822 airfoil at angle of incidence $\alpha = 2.79°$, the Mach number based on the free-stream conditions is M = 0.4 and the Reynolds number based on the free-stream conditions and the airfoil chord is $\mathrm{Re} = 6.5 \times 10^6$. No-slip adiabatic boundary conditions are applied on the airfoil and far-field boundary conditions are applied on the outer boundary.

The problem is solved, with the linear scheme on a sequence of unstructured grids of triangles obtained with a sequence of uniform refinements of the coarsest grid shown in Fig. 7, which is made of 4 048 elements. As standard practice in this work, an iso-parametric representation is used for the solution and the geometry. Due to the strong stretching of the boundary layer elements, some of the quadratic elements have curved boundaries non only on the airfoil wall but also at the interior. Solutions are considered to be at convergence when the L^2 norms of the residuals of all the variables are reduced by ten orders of magnitude.

In Fig. 8 are reported the contours of the computed Mach number and of the turbulent variable, $\chi = \mu_t^\star / \mu$, for the third order simulation on a fine grid, and Fig. 9 shows the pressure and friction coefficients along the airfoil computed with linear and quadratic elements on two different grids, such that the number of DOFs of the two simulations is the same ($N_{\mathrm{dof}} = 32\,784$); the respective iterative convergence histories are reported in Fig. 10.

For completeness, in Fig. 11 are reported the values of the lift and drag coefficients computed on different grids with linear and quadratic elements. Note how the use of quadratic elements allows a faster convergence with the mesh refinement of the lift and drag coefficients to their respective asymptotic values. In addition, Fig. 12 reports the errors

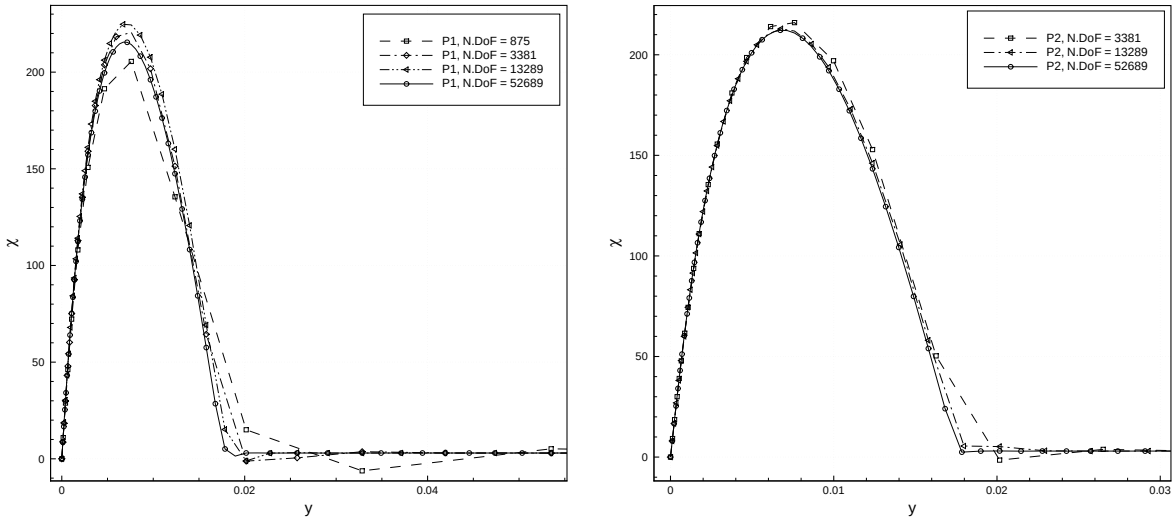

(a) (b)

Figure 6: Dimensionless turbulent working variable profiles in the boundary layer at the point $x = 0.97$ for the turbulent flow over a flat plate, with different grid resolutions and with linear (a) and quadratic (b) approximation of the solution.

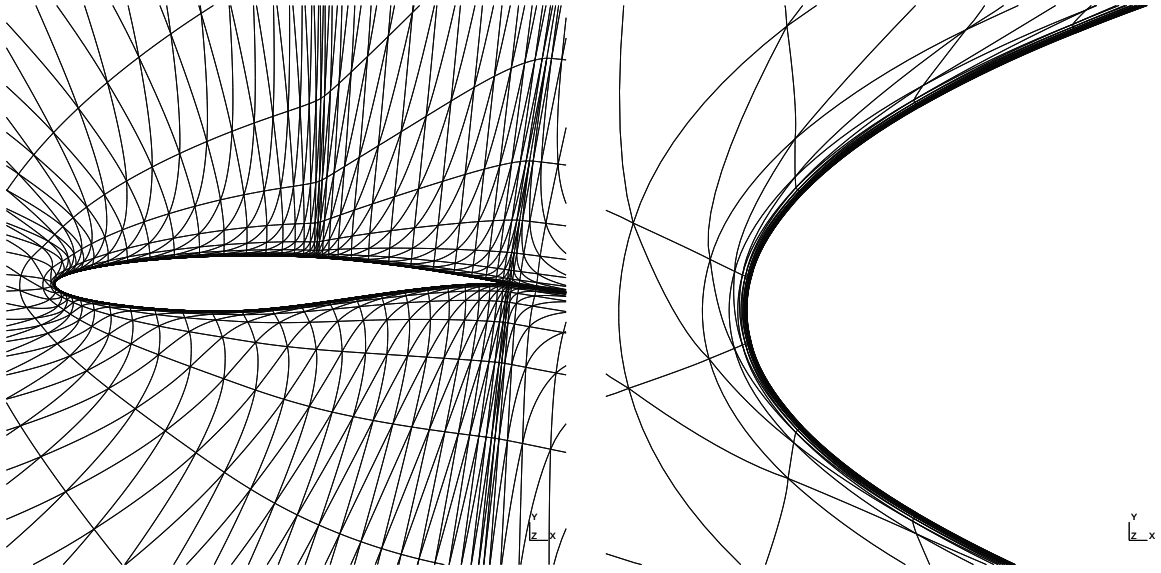

(a) (b)

Figure 7: An example of coarse grid used for the numerical simulation of a turbulent flow over the RAE2822 airfoil and a zoom of the mesh near the leading edge of the airfoil to show the curvilinear elements.

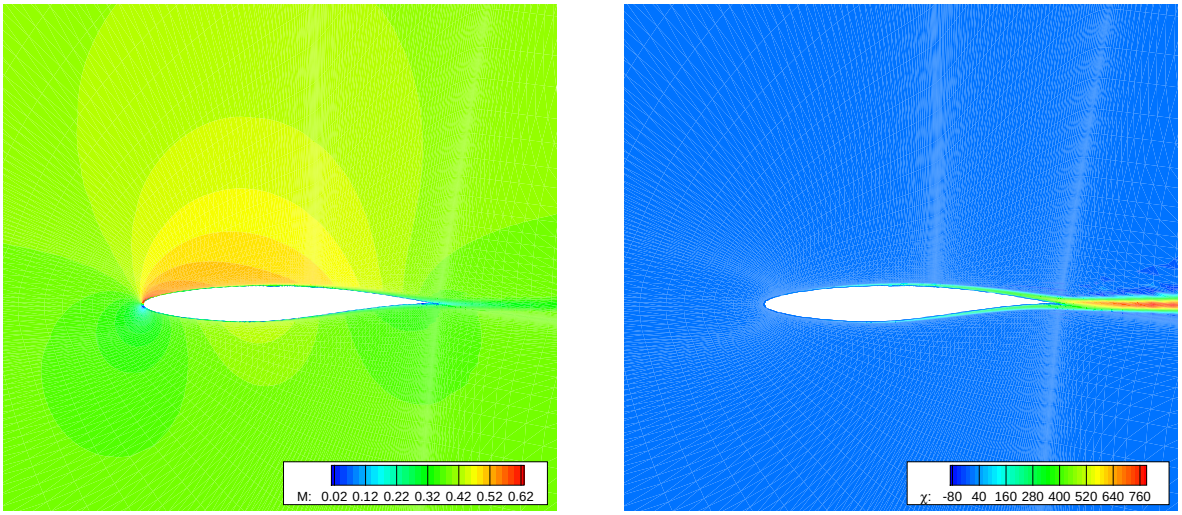

(a) (b)

Figure 8: Mach number (a) and turbulent working variable (b) contours for the subsonic flow over a RAE2822 airfoil discretized with quadratic elements.

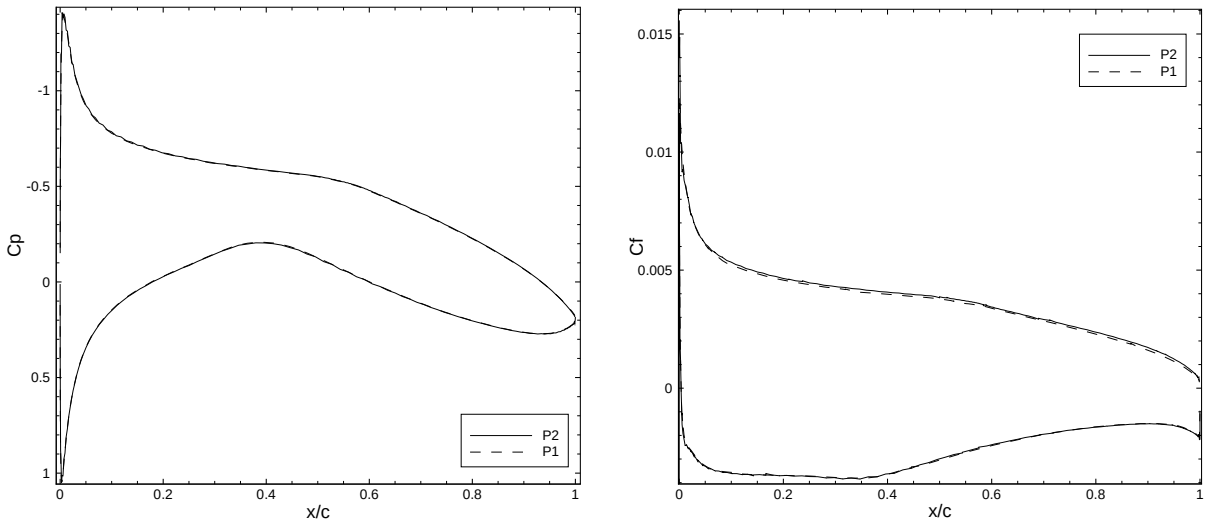

(a) (b)

Figure 9: Pressure (a) and friction (b) coefficient along the RAE2822 airfoil with linear and quadratic elements on two different grids, such that $N_{\text{dof}} = 32\,784$.

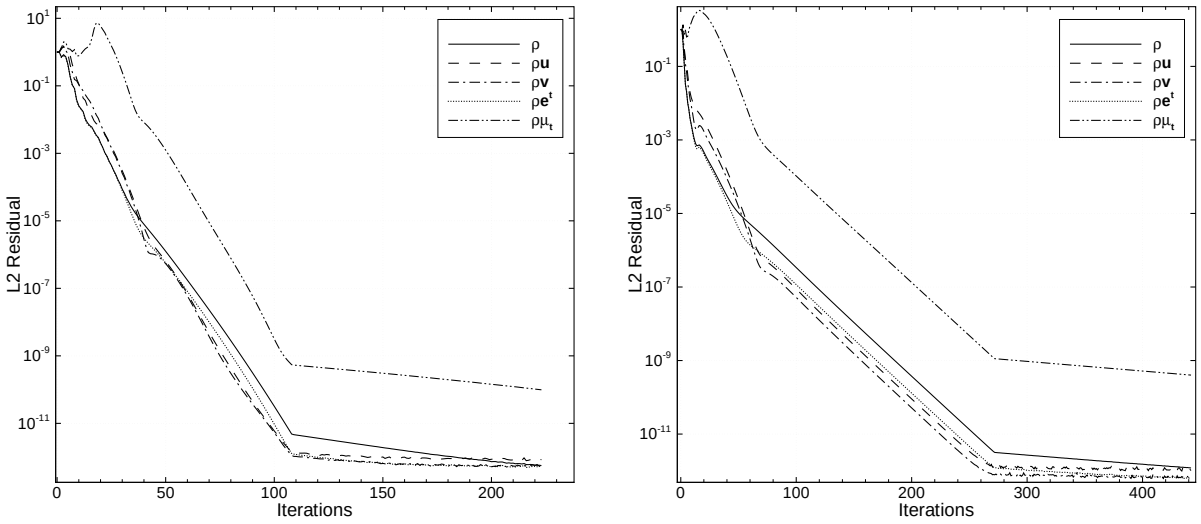

Figure 10: Iterative convergence for the simulation of the subsonic flow over the RAE2822 airfoil with linear (a) and quadratic (b) elements on two different grids, such that $N_{\text{dof}} = 32\,784$.

for the force coefficients; the error for the lift coefficient is computed as $err_{\text{CL}} = |c_{L_h} - c_{L_{\text{ex}}}|$, where c_{L_h} is the value of the lift coefficient computed numerically and $c_{L_{\text{ex}}}$ is a reference value obtained with a Richardson extrapolation [30] of the lift coefficients computed with quadratic elements. The same procedure is also used to compute the error on the drag coefficient. For the lift coefficient, it is clear the advantage of using a high-order approximation over a second order approach. For the drag coefficient, the difference between second and third order schemes reduces, but nevertheless the quadratic approximation of the solutions gives a smaller error for the same number of DOFs.

6.3. Transonic Flow over a RAE2822 Airfoil

In this test case a transonic, turbulent flow over a RAE2822 airfoil is considered. The free-stream Mach number is M = 0.734, the angle of incidence and the Reynolds number are the same of the previous test case, namely $\alpha = 2.79°$ and $\text{Re} = 6.5 \times 10^6$. In these conditions, the upper surface of the airfoil is characterized by the presence of a shock wave which impinges the boundary layer, generating a small recirculation bubble behind the shock. No-slip adiabatic boundary conditions are applied on the airfoil and far-field boundary conditions are applied on the outer boundary.

Due to the presence of the shock, the problem is discretized with the non-linear scheme. The L^2 norms of the residuals of the mean flow and of the turbulence equation are reduced at least by nine orders of magnitudes.

The same type of grids used in the previous test case is adopted here and three levels of refinement are considered. In Fig. 13 are reported the Mach number contours for the solution on the fine grid (64 768 elements) with quadratic elements, together with the iterative convergence history. Note that the shock is sharply captured with no oscillations.

In Fig. 14 are shown the pressure and the friction coefficients along the airfoil with linear elements on a finer grid and quadratic elements on a coarse grid, such that the number of DOFs in the two cases is the same: 32 784. The values of the computed pressure coefficient agree very well with the experimental data, especially with the quadratic discretization of the solution. The leading edge suction peak of the pressure is slightly under-predicted by the numerical simulations, due to the fact that the simulations have been performed in a fully turbulent regime. Also the friction coefficient agrees well with the experimental data. On the upper part of the airfoil, note the negative values of the friction coefficient just behind the shock obtained with the quadratic approximation of the solution, that identify the separation bubble induced by the shock.

Finally, in Fig. 15 are reported the values of lift and drag coefficients for linear and quadratic approximation of the solution with three levels of grid refinement.

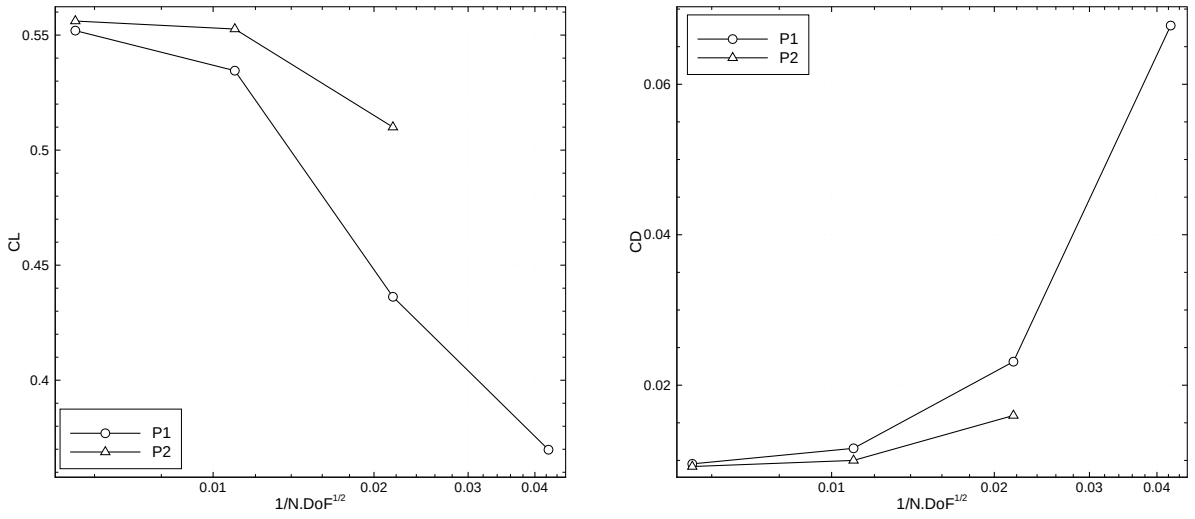

(a) (b)

Figure 11: Values of the lift (a) and drag (b) coefficients as function of the number of the degrees of freedom, for the subsonic turbulent flow over the RAE2822 airfoil, with linear and quadratic elements.

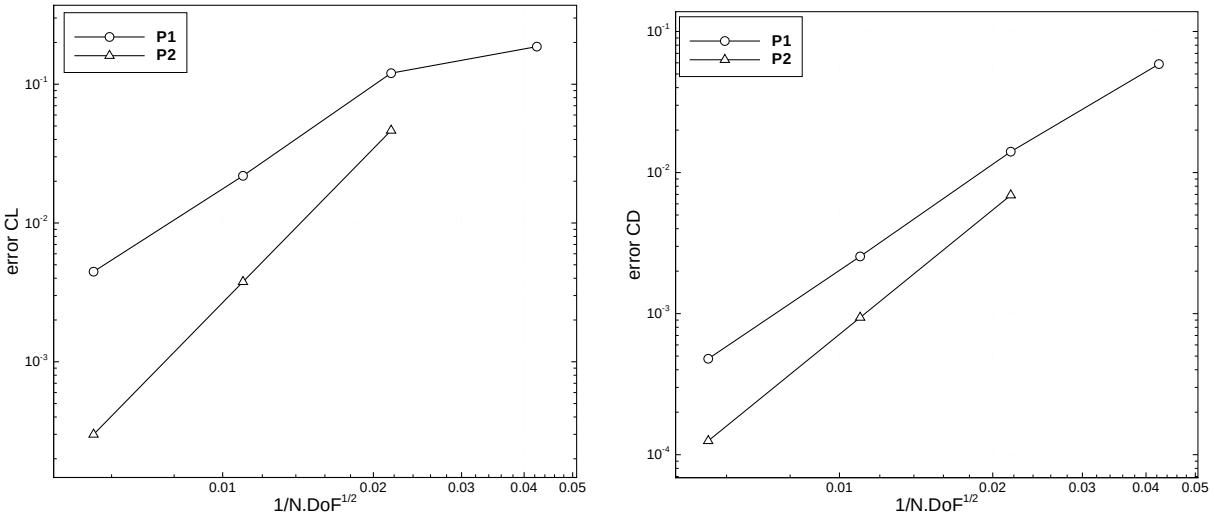

(a) (b)

Figure 12: Errors with linear and quadratic elements on the lift (a) and drag (b) coefficients for the subsonic turbulent flow over the RAE222 airfoil.

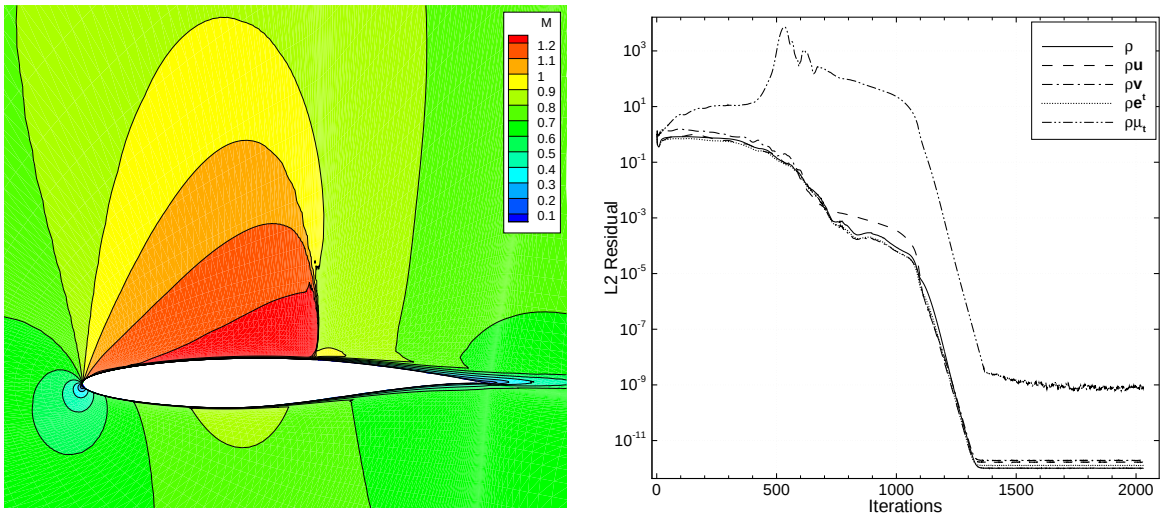

(a) (b)

Figure 13: Mach number contours (a) and iterative convergence history (b) for the transonic turbulent flow over a RAE2822 airfoil computed with quadratic elements.

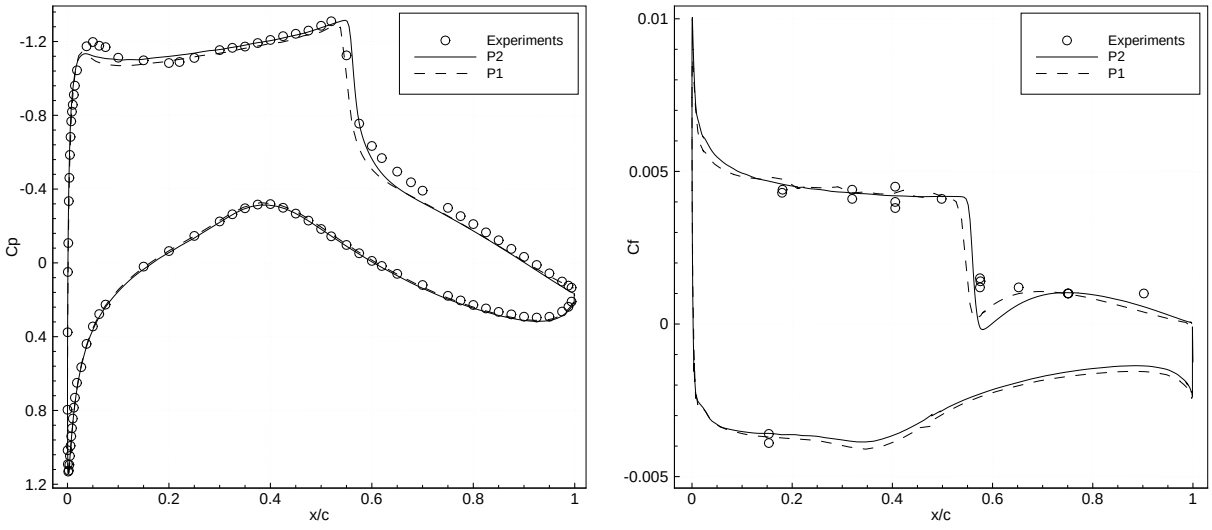

(a) (b)

Figure 14: Pressure (a) and friction (b) coefficients over the RAE2822 airfoil, for the transonic turbulent flow computed with linear and quadratic elements on two grids, such that $N_{\text{dof}} = 32\,784$.

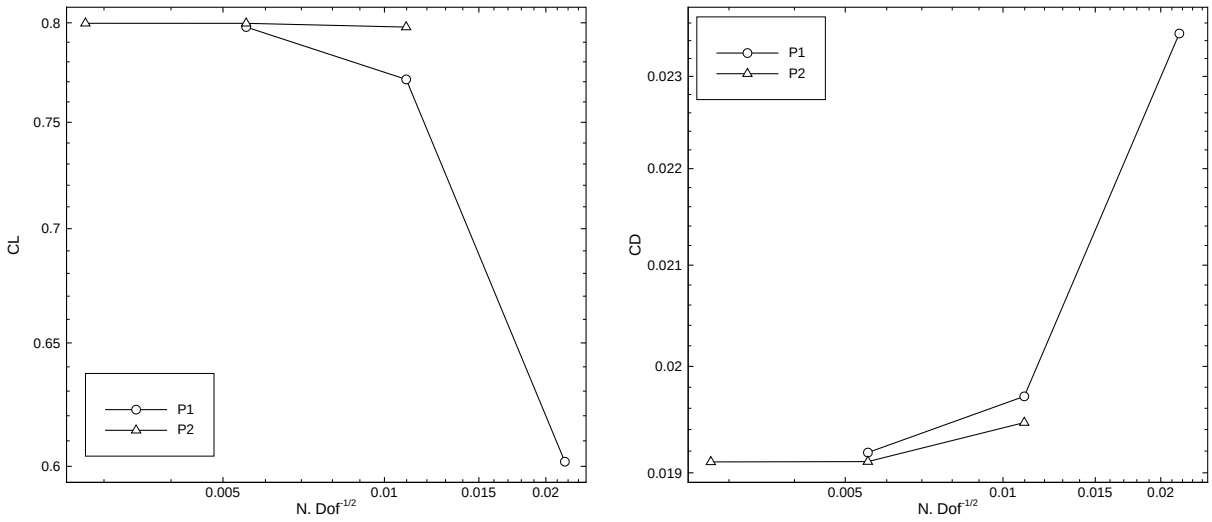

(a) (b)

Figure 15: Lift (a) and drag (b) coefficients on different grids, for the transonic turbulent flow over the RAE2822 airfoil, with linear and quadratic elements.

6.4. High-lift Multi-element Airfoil Configuration L1T2

The turbulent flow over the AGARD L1T2 high-lift multi-element airfoil is now considered. The geometry consists of a three-element airfoil configuration, the free-stream Mach number is M = 0.197, the angle of incidence is $\alpha = 20.18°$, and the Reynolds number based on the free-stream conditions and the retracted airfoil chord is Re = 3 520 000. No-slip adiabatic boundary conditions are applied on the airfoil and far-field boundary conditions are applied on the outer boundary.

The problem is solved with the linear scheme on a mesh of 33 338 triangles, shown in Fig. 16. This test case is particularly challenging due to the very high angle of attach and the flow complexity. The solution is considered to be at the steady state when the L^2 norms of the residuals of all the equations are reduced at least by nine orders of magnitude. In Fig. 17 is reported the converged history of the simulations with linear and quadratic elements. Note that order sequencing has been used to accelerate the convergence of the high-order simulation, *i.e.*, the solution computed with linear elements is used as initial solution for the simulation with quadratic elements. Despite the complexity of the flow-field, the non-linear LU-SGS scheme successfully converges to the steady state with both linear and quadratic elements.

In Fig. 18 are reported the Mach number contours computed with linear and quadratic elements. Clearly the high-order discretization drastically improves the accuracy of the solution compared to the second-order simulation. In Fig. 19 are reported the computed pressure and skin friction coefficients over the elements of the airfoil. The computed pressure coefficient is also compared against the experimental data [32]: a very good agreement between and numerical experimental data con be observed. For sake of completeness, in Table. 1 are listed the computed lift and drag coefficients, together with some values reported in literature.

6.5. ONERA M6 wing

The simulation of the transonic turbulent flow over the ONERA M6 wing is performed. The free-stream Mach number is M = 0.8395, the angle of incidence is $\alpha = 3.06°$ and the Reynolds number based of the free-stream values and the mean aerodynamic chord is Re = 11.72×10^6. The grid is composed by 123 444 tetrahedrons, and the mean height of elements on the wing in dimensionless units is approximately $y_1^+ = 5$. Far-field boundary conditions are applied on the outer part of the domain, symmetry boundary conditions are applied on the vertical plane that intersects the wing root and the wing surface is modeled as a non-slip adiabatic wall. In Fig. 20 are reported the grid used for the simulation and the pressure coefficient contours for the third-order simulation.

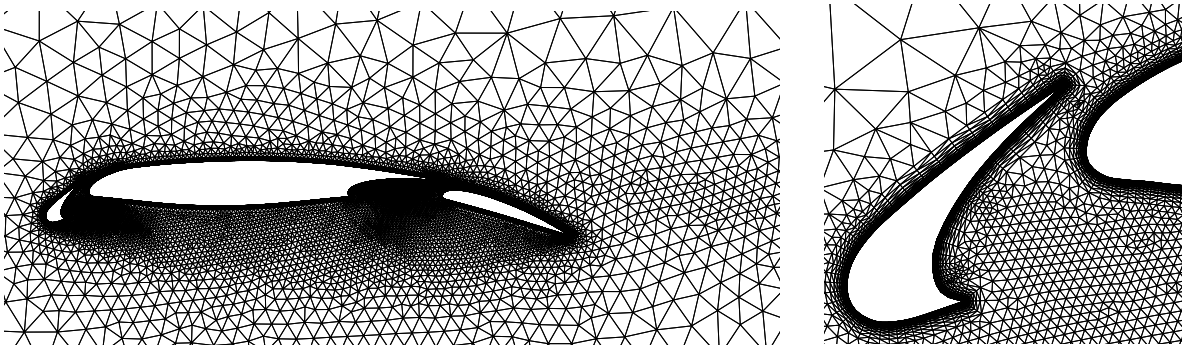

(a) (b)

Figure 16: Global view (a) of the computational mesh around the L1T2 multi-element airfoil, and zoom (b) near the slat and the main element.

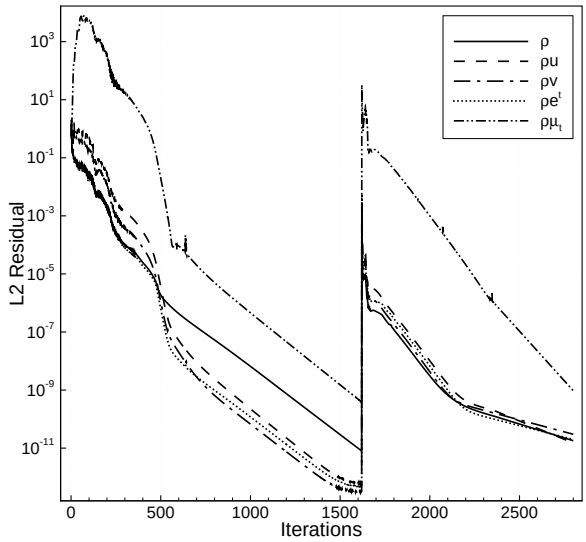

Figure 17: Convergence history for the simulations over the L1T2 multi-element airfoil with linear and quadratic elements.

	N. DOFs	Cl	Cd
linear elements	16 943	3.8487	0.132940
quadratic elements	67 226	4.0002	0.080555
DG P1, SA [33]	265 311	4.055891	0.067782
DG P2, SA [33]	553 707	4.049804	0.066554
DG P3, SA [33]	945 930	4.048049	0.066471
DG P4, SA [33]	1 441 980	4.047551	0.066402
FV, k-ω EARSM [34]	114 908	4.08	0.068
Experiment [32]	-	4.11	0.068

Table 1: Computed force coefficients and reference values reported in literature for the simulation of the flow over the L1T2 multi-element airfoil.

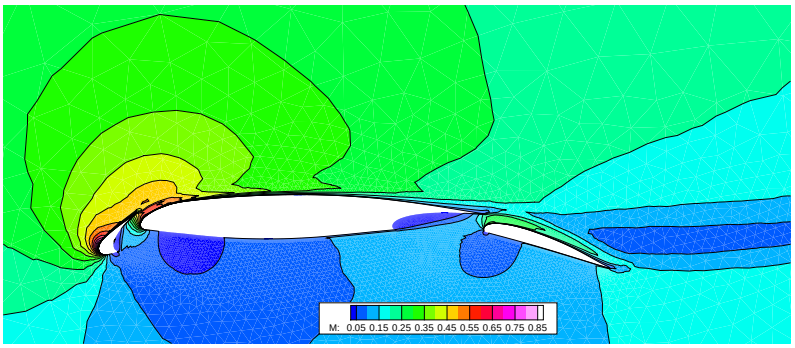

(a)

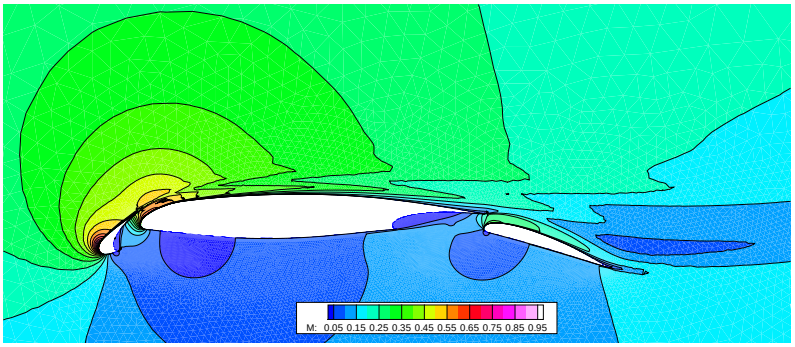

(b)

Figure 18: Mach number contours for the flow over the L1T2 multi-element airfoil with linear (a) and quadratic (b) elements.

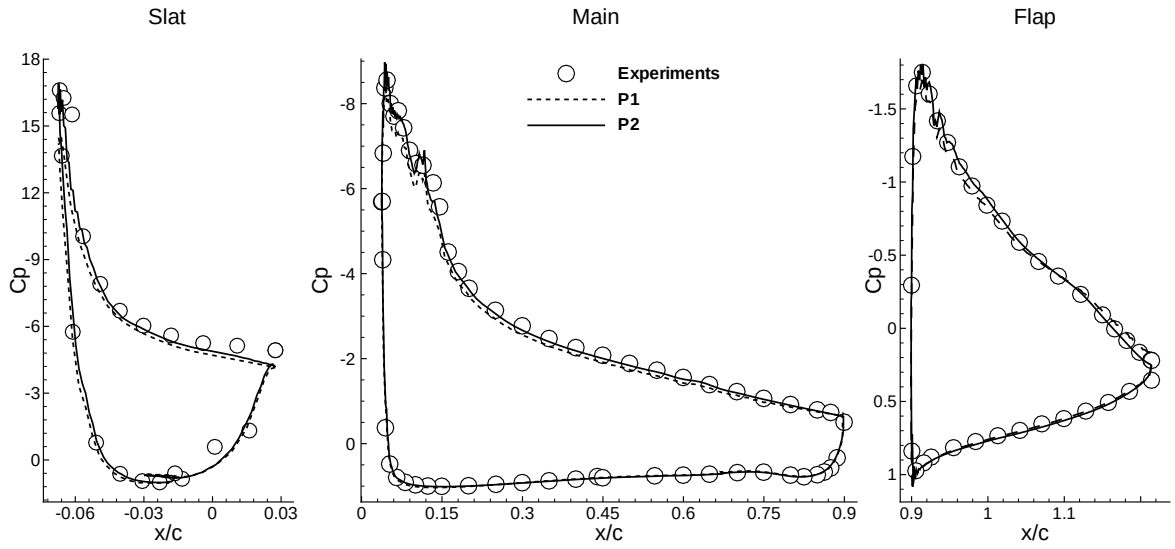

(a)

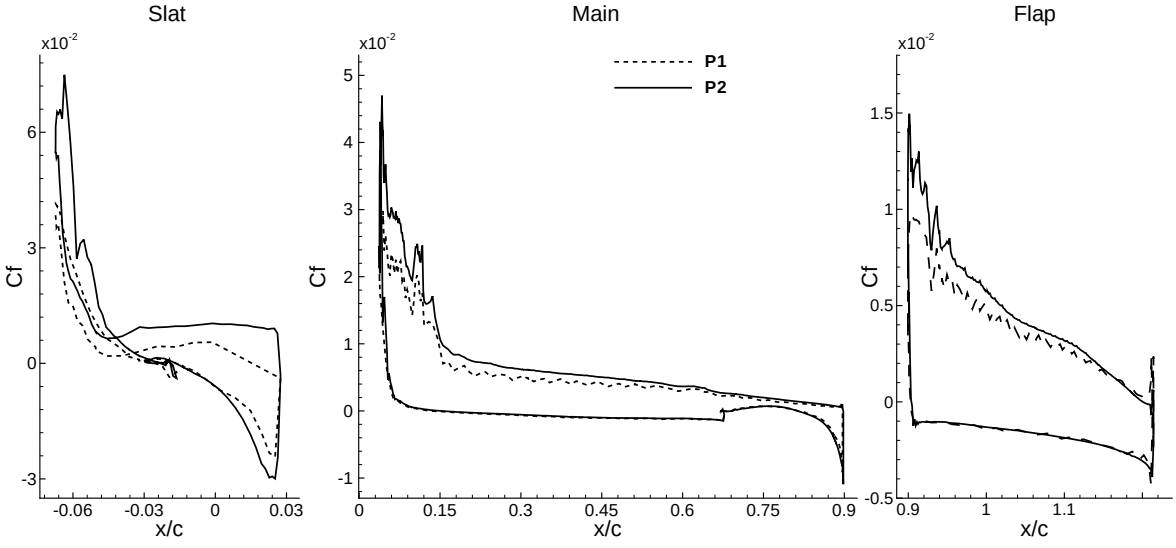

(b)

Figure 19: Pressure (a) and skin friction (b) coefficients for the flow over the L1T2 multi-element airfoil.

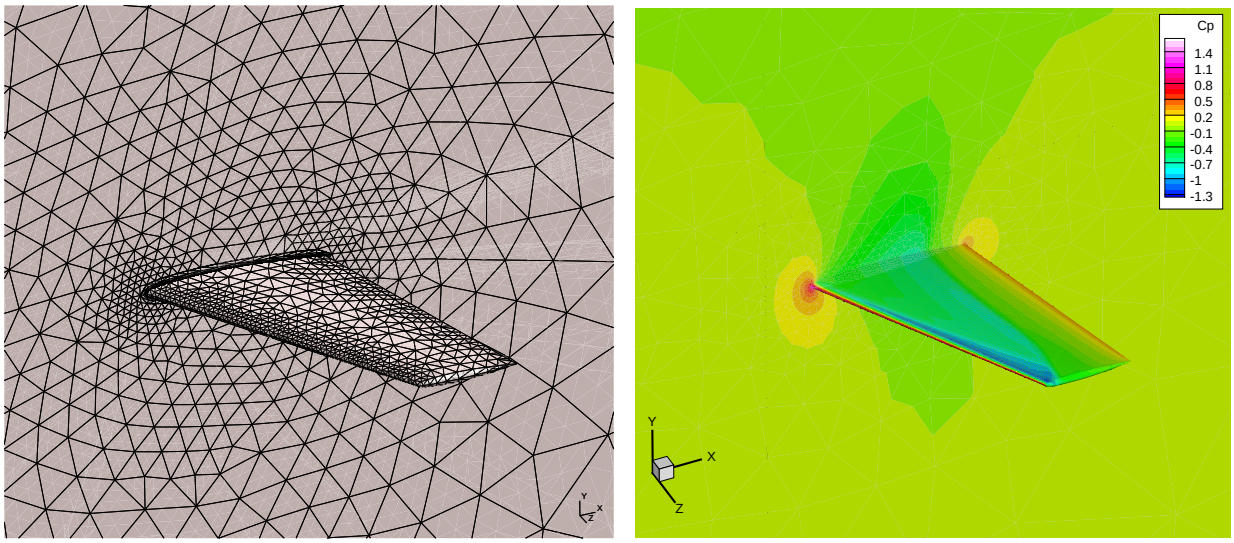

(a) (b)

Figure 20: Computational mesh used for the simulation of the turbulent flow over the M6 wing (a) and pressure coefficient contours (b) for the third-order simulation.

The non-linear solver has been used to discretize the governing equations. Convergence is considered achieved when the L^2 norms of the residuals of all the equations are reduced by eight orders of magnitude. Simulations have been performed in parallel on 64 processors.

In figure Fig. 21, the values of the pressure coefficient for the third-order simulation at different stations along the span-wise direction of the wing are compared against the experimental data. Despite the quite coarse mesh, a good agreement with the experimental data is obtained and even the lambda shock is well represented. However, a finer grid would be required to better capture the shock structure at wing tip and also to better resolve the complex shock-boundary layer interaction occurring here.

6.6. NASA Delta wing

The simulation of the subsonic turbulent flow over the NASA 65° sweep delta wing with a medium radius leading edge is now considered. The free-stream Mach number is $M = 0.4$, the angle of attach is $\alpha = 13.3°$ and the Reynolds number based on the free-stream conditions and the mean aerodynamic chord is $\mathrm{Re} = 3 \times 10^6$. This test case has been computed with the linear scheme using linear and quadratic approximation of the solution, on a grid of 1 145 797 tetrahedrons (Fig. 22-a). For this test case only a linear approximation of the geometry is available. Simulations has been performed in parallel using 96 cores. With linear elements the L^2 norms of the residuals have been reduced by 8 orders of magnitude, while with quadratic elements they could non be reduced by more than 5 orders of magnitude. This is issue is probably due to to the poor representation of the wing geometry.

In Fig. 22-b are shown, for the solution with P2 elements, the contours of the pressure coefficients and slices of the turbulent working variable at different stations along and behind the wing. Starting from the apex of the wing, the flow around the rounded leading edge is initially attached. Further downstream the flow separates and the inner vortex is generated, eventually a separation of the shear layer occurs further downstream at the leading edge and the outer vortex is generated. The resulting vortex structure is then transported behind the wing.

The comparison with the experimental results [35] is shown in Fig. 23. The agreement between the numerical results and the experimental data is mildly good, considering the quite coarse mesh and the simple turbulent model used. Note also that capturing the correct position of the vortices separation and reattachment points is quite challenging for this test case, as observed in other numerical simulations [36].

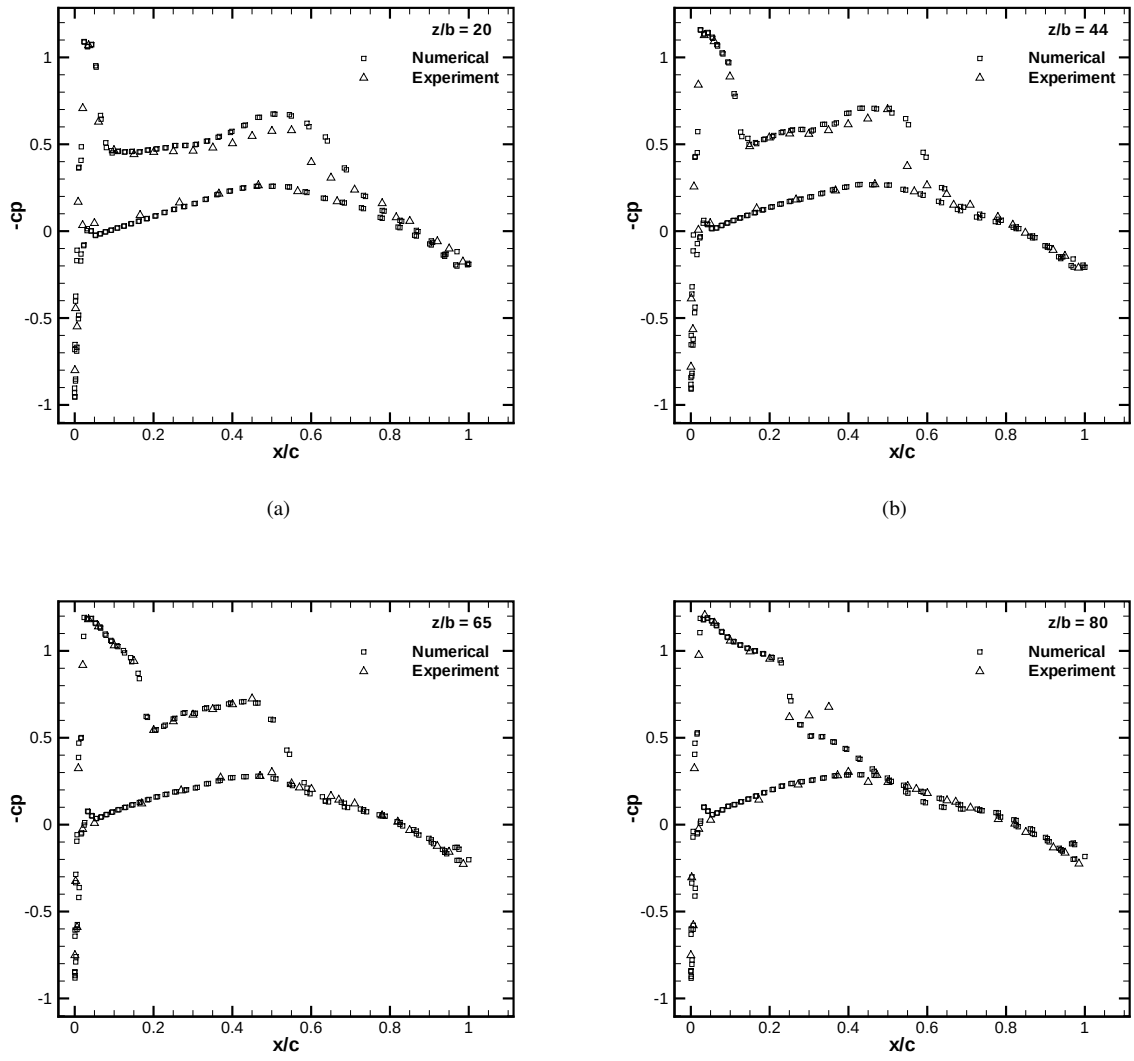

Figure 21: Pressure coefficient distribution at different span-wise locations over the M6 wing, for the third-order simulation.

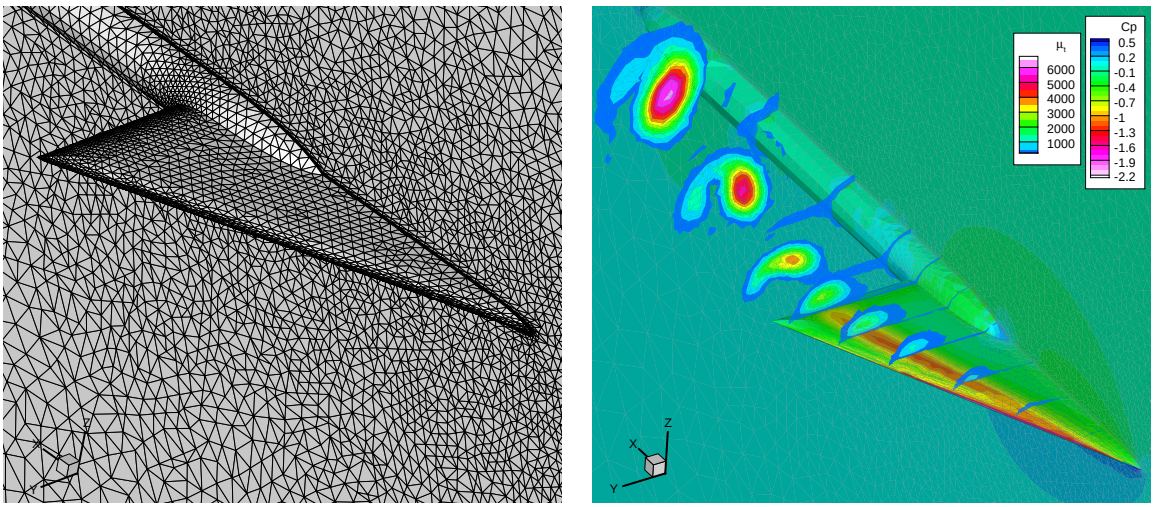

(a) (b)

Figure 22: 3D turbulent subsonic flow over a delta wing. Left: the mesh used, right pressure coefficient contours and slices of the turbulent working variable, with P2 elements.

7. Conclusions

This paper presents a high-order Residual Distribution discretization method for the solution of the multidimensional RANS equations. A modified form of the Spalart-Allmaras turbulence model has been introduced, which is strongly coupled with the mean flow equations. The numerical scheme relies on a continuous approximation of the solution and its gradient. A key aspect that emerged from previous works is that the reconstructed gradient of the numerical solution must have the same accuracy of the discrete solution. The so-called Super-convergent Patch Recovery method has been used to obtain accurate values of the gradient of the numerical solution, keeping the computational stencil compact.

The possibility to construct non-linear schemes within the Residual Distribution framework makes these schemes very attractive, because shocks and smooth solution can be handled within the same numerical scheme without introducing any tuning parameter or additional stabilization terms. On the other hand, linear schemes can be still useful when smooth solutions are expected.

The non-linear LU-SGS solver has been used to construct a robust implicit scheme which has been successfully used to make the scheme converge to the steady state for both the mean flow equation and the turbulent model.

The accuracy of the numerical schemes has been tested with standard test cases: the turbulent flow over the flat plate, the subsonic and transonic flow over the RAE2822 airfoil. The proposed numerical approach has been subsequently used to perform more challenging simulations like the two-dimensional flow over the high-lift multi-element airfoil and three-dimensional cases like the the transonic flow over the M6 wing and the subsonic flow over a delta wing.

References

[1] J. A. Ekaterinaris, High-order accurate, low numerical diffusion methods for aerodynamics, Progress in Aerospace Sciences 41 (2005) 192–300.

[2] B. Cockburn, G. Karniadakis, C. Shu, Discontinuous Galerkin methods: theory, computation and application, Lecture notes in computational science and engineering, Springer, Berlin, 2000.

[3] H. Deconinck, M. Ricchiuto, Residual distribution schemes: Foundations and analysis, in: Encyclopedia of Computational Mechanics, John Wiley & Sons, Ltd, 2004.

[4] T. J. R. Hughes, Recent progress in the development and understanding of supg methods with special reference to the compressible euler and navier-stokes equations, International Journal for Numerical Methods in Fluids 7 (1987) 1261–1275.

[5] V. Selmin, J. Donea, L. Quartapelle, Finite element methods for nonlinear advection, Computer Methods in Applied Mechanics and Engineering 52 (1985) 817 – 845.

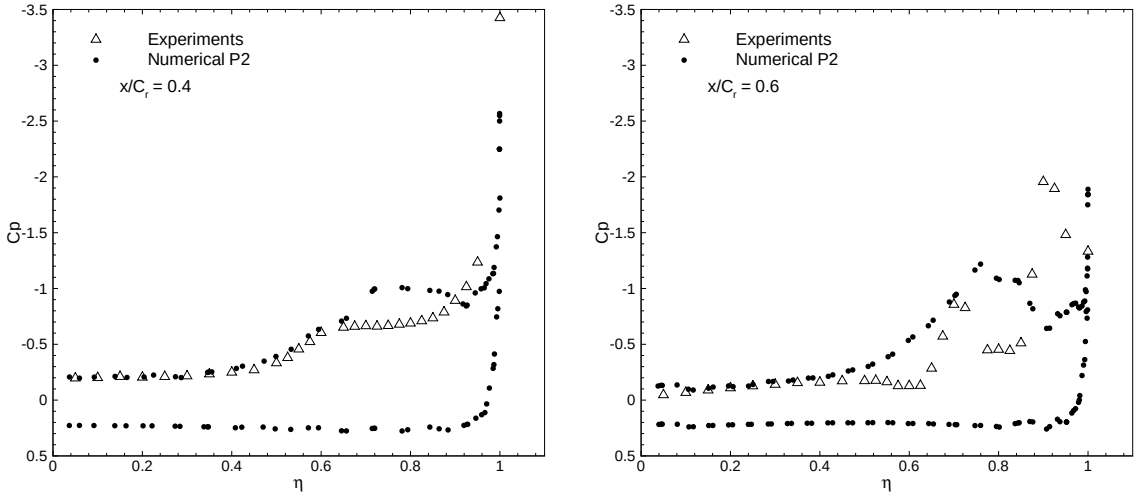

(a)

(b)

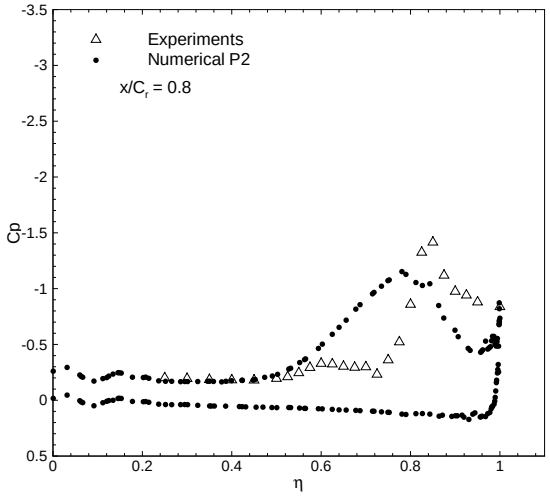

(c)

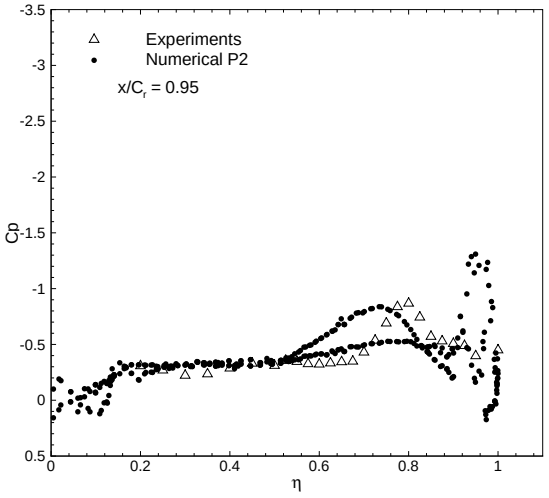

(d)

Figure 23: 3D turbulent subsonic flow over a delta wing. Pressure coefficients distribution at different wing sections. Comparison between the quadratic solution and the experimental data.

[6] R. Abgrall, Essentially non-oscillatory residual distribution schemes for hyperbolic problems, Journal of Computational Physics 214 (2006) 773–808.
[7] R. Abgrall, D. De Santis, M. Ricchiuto, High order preserving residual distribution schemes for advection-diffusion scalar problems on arbitrary grids, SIAM Journal on Scientific Computing (2013, Accepted).
[8] O. C. Zienkiewicz, J. Z. Zhu, A simple error estimator and adaptive procedure for practical engineerng analysis, International Journal for Numerical Methods in Engineering 24 (1987) 337–357.
[9] O. C. Zienkiewicz, J. Z. Zhu, The superconvergent patch recovery and a posteriori error estimates. part 2: Error estimates and adaptivity, International Journal for Numerical Methods in Engineering 33 (1992) 1365–1382.
[10] R. Abgrall, D. De Santis, Linear and non-linear high order accurate residual distribution schemes for the discretization of the steady compressible navier-stokes equations, Journal of Computational Physics (2014, under review).
[11] P. R. Spalart, S. R. Allmaras, A one-equation turbulence model for aerodynamic flows, Recherche Aerospatiale 1 (1994) 2244–2553.
[12] S. R. Allmaras, Multigrid for the 2-D Compressible Navier-Stokes Equations, in: 14th Computational Fluid Dynamics Conference, AIAA Paper 2011-3407, 2011.
[13] T. A. Oliver, High-Order, Adaptive, Discontinuous Galerkin Finite Element Method for the Reynolds-Averaged Navier-Stokes Equations, Ph.D. thesis, Massachusetts Institute of Technology, 2008.
[14] D. Moro, N. C. Nguyen, J. Peraire, Navier-Stokes solution using hybridizable discontinuous Galerkin methods, in: 20th AIAA Computational Fluid Dynamics Conference, AIAA Paper 2011-3407, 2011.
[15] S. R. Allmaras, F. T. Johnson, P. R. Spalar, Modifications and Clarifications for the Implementation of the Spalart-Allmaras Turbulence Model, in: Seventh International Conference on Computational Fluid Dynamics (ICCFD7), ICCFD7-4202, 2012.
[16] A. Crivellini, V. D'Alessandro, F. Bassi, A Spalart-Allmaras turbulence model implementation in a discontinuous Galerkin solver for incompressible flows, Journal of Computational Physics 241 (2013) 388 – 415.
[17] R. Abgrall, P. L. Roe, High-order fluctuation schemes on triangular meshes, Journal of Scientific Computing 19 (2003) 3–36.
[18] H. Luo, L. Luo, R. Nourgaliev, V. a. Mousseau, N. Dinh, A reconstructed discontinuous Galerkin method for the compressible NavierStokes equations on arbitrary grids, Journal of Computational Physics 229 (2010) 6961–6978.
[19] B. van Leer, S. Nomura, Discontinuous galerkin for diffusion, in: Proceedings of 17th AIAA computational fluid dynamics conference, AIAA-2005-5108, 2005.
[20] R. Abgrall, A. Larat, M. Ricchiuto, Construction of very high order residual distribution schemes for steady inviscid flow problems on hybrid unstructured meshes, Journal of Computational Physics 230 (2011) 4103–4136.
[21] B. Cockburn, C.-W. Shu, The Local Discontinuous Galerkin Method for Time-Dependent Convection-Diffusion Systems, SIAM Journal on Numerical Analysis 35 (1998) 2440.
[22] O. Zienkiewicz, R.L.Taylor, Finite Element Method (5th Edition) Volume 1 - The Basis, Elsevier, 2000.
[23] L. R. Herrmann, Interpretation of finite element procedure as stress error minimization procedure, Journal of the Engineering Mechanics Division 98 (1972) 1330–1336.
[24] Y. Sun, Z. Wang, Y. Lun, Efficient implicit non-linear lu-sgs approach for compressible flow computation using high-order spectral difference method, Communications in computational physics 5 (2009) 760–778.
[25] M. Parsani, G. Ghorbaniasl, C. Lacor, E. Turkel, An implicit high-order spectral difference approach for large eddy simulation, Journal of Computational Physics 229 (2010) 5373 – 5393.
[26] T. Haga, K. Sawada, Z. J. Wang, An Implicit LU-SGS Scheme for the Spectral Volume Method on Unstructured Tetrahedral Grids, Communications in Computational Physics 6 (2009) 978–996.
[27] M. Tidiriri, Preconditioning techniques for the Newton-Krylov solution of compressible flows, Journal of Computational Physics 132 (1997) 51–61.
[28] R. Abgrall, D. De Santis, M. Ricchiuto, High order residual distribution scheme for rans equations, in: Seventh International Conference on Computational Fluid Dynamics, ICCFD7-2802, 2012.
[29] K. Wieghardt, W. Tillman, On the turbulent friction layer for rising pressure, Technical Report 1314, NACA, 1951.
[30] P. J. Roache, Verification and Validation in Computational Science and Engineering, Hermosa Publishers, 1998.
[31] S. B. Pope, Turbulent Flows, Cambridge University Press, 2000.
[32] A. G. F. A. RESEARCH, D. N.-S.-S. F. CE), A Selection of Experimental Test Cases for the Validation of CFD Codes. Volume 2, Defense Technical Information Center, 1994.
[33] N. K. Burgess, D. J. Mavriplis, High-order Discontinuous Galerkin Methods for Turbulent High-lift Flows, in: Seventh International Conference on Computational Fluid Dynamics (ICCFD7), ICCFD7-4202, 2012.
[34] C. L. Rumsey, T. B. Gatski1, S. X. Ying, A. Bertelrud, Prediction of high-lift flows using turbulent closure models, AIAA Journal 36 (1998) 765–774.
[35] J. L. J. Chu, Experimental surface pressure data obtained on 65° delta wing across Reynolds number and Mach number ranges, NASA Technical Memorandum 4645.
[36] A. Schutte, H. Ludeke, Numerical investigations on the VFE-2 65-degree rounded leading edge delta wing using the unstructured DLR TAU-Code, Aerospace Science and Technology 24 (2013) 56 – 65.